Predicting the Corona for the 21 August 2017 Total Solar Eclipse

Zoran Mikić[1,*], Cooper Downs[1], Jon A. Linker[1], Ronald M. Caplan[1], Duncan H. Mackay[2], Lisa A. Upton[3], Pete Riley[1], Roberto Lionello[1], Tibor Török[1], Viacheslav S. Titov[1], Janvier Wijaya[1], Miloslav Druckmüller[4], Jay M. Pasachoff[5,6], and Wendy Carlos[7]

[1]Predictive Science, Inc., San Diego, CA 92121, USA
[2]School of Mathematics and Statistics, University of St Andrews, St Andrews, Fife, KY16 9SS, UK
[3]High Altitude Observatory, National Center for Atmospheric Research, Boulder, CO 80301, USA
[4]Institute of Mathematics, Faculty of Mechanical Engineering, Brno University of Technology, Czech Republic
[5]Williams College–Hopkins Observatory, Williamstown, MA 01267, USA
[6]Carnegie Observatories, Pasadena, CA 91101, USA
[7]New York City, NY 10003, USA
[*]mikicz@predsci.com

The total solar eclipse that occurred on 21 August 2017 across the United States provided an opportunity to test a magnetohydrodynamic model of the solar corona driven by measured magnetic fields. For the first time we used a new heating model based on the dissipation of Alfvén waves, and a new energization mechanism to twist the magnetic field in filament channels. We predicted what the corona would look like, one week before the eclipse. Here we describe how this prediction was accomplished, and we show that it compared favorably with observations of the eclipse in white light and extreme ultraviolet. The model allows us to understand the relationship of observed features, including streamers, coronal holes, prominences, polar plumes, and thin rays, to the magnetic field. We show that the discrepancies between the model and observations arise from limitations in our ability to observe the Sun's magnetic field. Predictions of this kind provide opportunities to improve the models, forging the path to improved space weather prediction.

Background

Eclipses have long been a source of wonder and fascination, but they also have a unique place in the scientific discovery process. On 21 August 2017, a celestial spectacle delighted millions of people across the United States, as a total solar eclipse swept across the country. It provided an opportunity to test our understanding of the physics of the solar corona[1–3], the region of the Sun's atmosphere where the gas is heated to over a million degrees by processes that are still not fully understood[4–6]. During totality a solar eclipse reveals the faint corona that is normally hidden from view, exposing intricate structures that are shaped by the magnetic field, including streamers, polar plumes, rays, and prominences. The coronal magnetic field is the source of the energy that is released during the solar flares[7] and coronal mass ejections that can damage Earth-orbiting satellites and cause power outages. It dominates the structure and dynamics of the corona, but is difficult to observe above the photosphere and chromosphere. It is of intense scientific interest to understand how the magnetic field emerges from beneath the Sun's surface, how it evolves, when it is about to erupt, and how such ejections travel through interplanetary space. These eruptions have the potential to trigger a geomagnetic storm when they interact with the Earth's magnetic field.

It is only through detailed three-dimensional (3D) modeling of the solar corona that we can link ob-

servations of the Sun's magnetic field in the photosphere to the coronal structures that are unveiled during an eclipse. Complementary measurements of extreme ultraviolet (EUV) and X-ray emission from space offer an additional perspective. White-light observations of the corona are made routinely from ground-based observatories and spaceborne coronagraphs, but neither can image the lowest layers of the corona, or capture the finest details that are observed during eclipses (though future space coronagraphs promise to narrow this gap[8]). Consequently, even with today's detailed space measurements of the Sun, eclipses play a unique role in this discovery process[9–11], especially since the expense of the instrumentation required is relatively modest.

It has been said that prediction is the ultimate test of a scientific theory. It was during the 1919 eclipse that Eddington and colleagues verified Einstein's theory of general relativity to great acclaim, confirming a prediction for the shift in the apparent position of stars by warping of space by the Sun[12] (though the accuracy of the measurement is not without controversy[13–15]). Our group has made routine predictions of the eclipse corona for over two decades[16–18], during which time our models have improved steadily as a result of dramatic advances in computing power, but also through enhancements in the physics of the models. These improvements were driven in part by comparisons with eclipse predictions. In the future, these and similar models are expected to improve the forecasting of solar storms. In this article, we describe a prediction of the solar corona using a computer model that tests recent advances in theory and modeling with modern observations. The model employs two key innovations: a physics-based formulation that describes the heating of the corona over a broad range of conditions, and a novel approach for energizing the coronal magnetic field on global scales. A related prediction of this eclipse with a different model has also been made[19], and is discussed below.

Predicting the Eclipse Corona

We predicted the structure of the corona one week prior to the eclipse, using a 3D magnetohydrodynamic (MHD) model to compute the interaction of the solar wind with the Sun's magnetic field (see Methods). It tracks the exchange of energy between coronal heating, radiative losses, and thermal conduction along the magnetic field, and is fed by measurements of the magnetic field in the photosphere[20–22]. We used spaceborne measurements of the photospheric magnetic field from the Helioseismic and Magnetic Imager (HMI)[23] aboard the Solar Dynamic Observatory (SDO)[24], and a wave-turbulence-driven (WTD) model to heat the corona via low-frequency Alfvén waves launched in the chromosphere[25–27]. A fraction of the outward-directed waves interact with reflected waves[28] and dissipate, heating the corona.

Eclipses reveal the lowest regions of the solar corona, where prominences are often seen, embedded at the base of coronal streamers and pseudostreamers[29]. Several prominences were observed during the 21 August 2017 eclipse, as is typical during this declining phase of the solar cycle. These dense, cold structures are believed to be supported by magnetic fields in filament channels[30–32]. When a prominence is present within a streamer, it tends to produce an "inflated" appearance because of the extra magnetic pressure from the magnetic field (see Supplementary Figure 6). To model these features, we implemented a technique to introduce highly sheared magnetic fields in these channels, at locations that were determined by examining animated images of EUV emission observed by the Atmospheric Imaging Assembly (AIA)[33] on SDO (see Supplementary Figure 5). This process increased the free magnetic energy, "energizing" the corona, as described in the Methods section.

As a boundary condition on our model we used photospheric magnetic fields derived from synoptic HMI measurements of the longitudinal (line-of-sight) component of the magnetic field, including data from Carrington rotation (CR) 2192, starting on 16 July 2017, combined with "Near Real Time" data from CR 2193, measured up to 12:00 UT on 11 August 2017, ten days prior to totality. (The composite

synoptic chart is shown in Supplementary Figure 2.) The parameters for the model, including the driving Alfvén wave amplitude, were selected based on runs made during the previous two months (as discussed in the Methods section, and summarized in Supplementary Figure 1). The calculation was begun on 11 August 2017, starting from one of these previous solutions. The corona was relaxed towards equilibrium by advancing the model for 60 hours of solar time in a dedicated queue at NASA's Advanced Supercomputing Center. At the final stage of our calculation, we introduced magnetic shear in filament channels, relaxing the corona for another 8 hours. These runs took a total of 54 hours of real time to advance 68 hours of solar time.

Since the corona responds to changes in the photospheric magnetic field, the accuracy of a prediction deteriorates over time. We would expect better accuracy during this declining phase of the solar cycle, when the Sun's magnetic field changes more slowly than at solar maximum, and this was indeed the case. Flux transport models have promise in improving the accuracy of the evolving photospheric magnetic field. Indeed, the Surface Flux Transport (SFT) model has been used in conjunction with a potential field source-surface (PFSS) model to predict the structure of the coronal magnetic field for this eclipse[19]. While this simpler model does not predict coronal density and temperature, and does not produce non-potential coronal magnetic fields, it can be carried out rapidly. The flux transport model that we used to identify energized filament channels (see the Methods section) employs a magnetofrictional model in the corona, and produces nonpotential coronal fields[34].

After completing the calculation, we synthesized observables that can be compared directly with observations taken during the eclipse. From the predicted electron density we computed the total and polarized brightness in white light[35], quantities that are principally measured during eclipses. Polarized brightness can be useful in separating the significantly polarized K-corona, of solar origin, from the largely unpolarized fainter outer F-corona, whose main contribution is from interplanetary dust[36]. Using the distribution of temperature, we computed the EUV emission expected in various channels of the AIA telescope, as well as soft X-ray emission[18,22,37]. We also visualized the squashing factor[38] Q that emphasizes the fine spatial scales in the magnetic field, as discussed in the Methods section.

Comparison with Eclipse Observations

Our prediction was tested against photographs of the eclipse and spaceborne observations. Overall, the model predicted the general appearance of the corona, though many details were different. The principal large-scale streamers that visually dominate the eclipse corona were predicted accurately. Figure 1 shows a comparison between two eclipse images and several predicted quantities from the MHD simulation. A series of photographs taken at different exposures by the Solar Wind Sherpas eclipse expedition in Mitchell, Oregon, were combined digitally and enhanced[39] to emphasize the finest details in the corona (Fig. 1a). A different series of 14 photographs taken in Salem, Oregon, by the Williams College expedition, were assembled digitally (Fig. 1b) as described in the Methods section. It is difficult to produce a simulated image of what the eye sees during an eclipse, because of the accommodation of the eye to the wide range of brightness in the corona, but in our personal experience, it is likely to between Fig. 1a and Fig. 1b.

These two images show features that resemble those in the predicted white-light polarized brightness (pB) (Fig. 1c). We detrended pB radially using the Newkirk vignetting function to bring out the faint intensity in the outer corona. This mimics the effect of a radially-graded filter that was used in past decades during a time when eclipse photography employed analog techniques[36,40]. The radial variation of intensity between the processed photographs and this pB image is therefore arbitrary, and should not be considered when comparing these images—only a latitudinal comparison of intensity is meaningful.

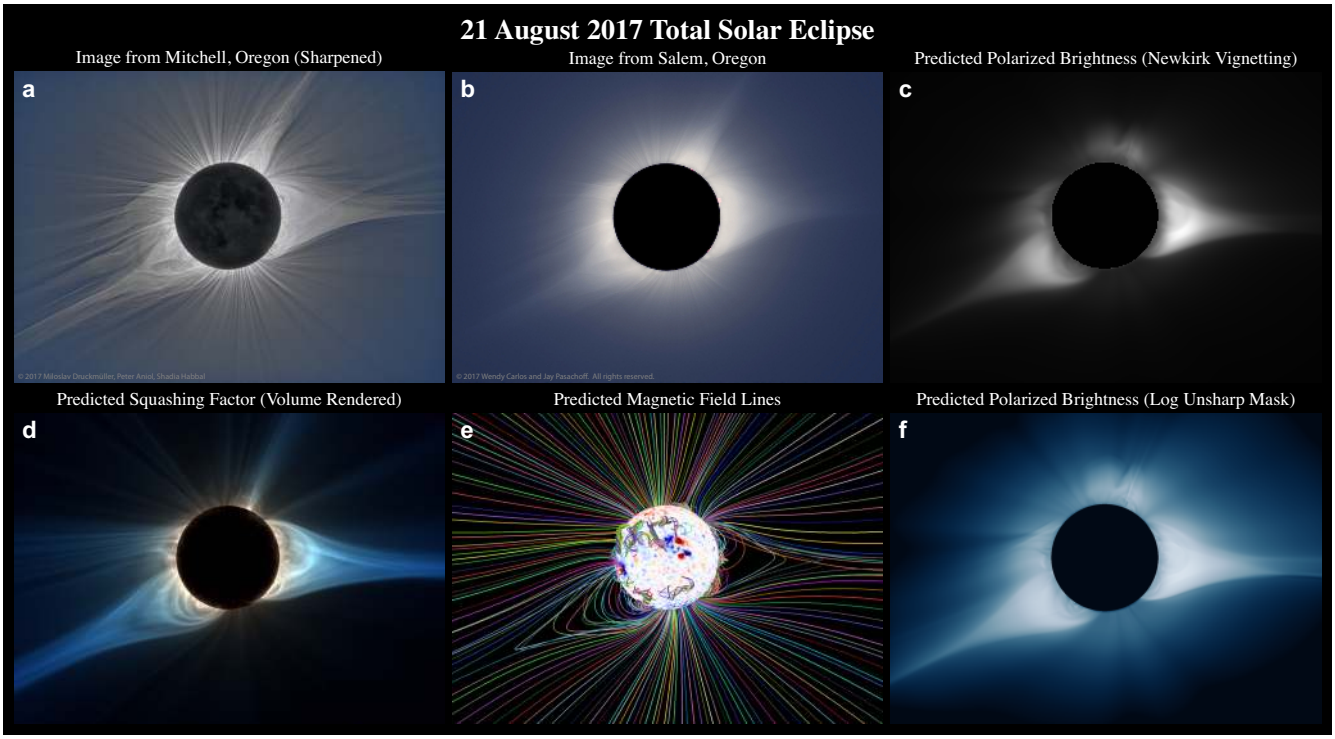

Figure 1. Comparison between the observed and predicted eclipse corona. The images are oriented with terrestrial north up; solar north is 18.2° counterclockwise from the vertical.

For an animation of pB at different longitudes see Supplementary Video 1. An alternate depiction of the coronal structure is obtained by using an "unsharp mask" on pB and displaying the result using a logarithmic scaling (Fig. 1f).

Polar plumes, which are visible in the polar regions (Fig. 1a), are seen to align with the magnetic field lines (Fig. 1e), as shown in Supplementary Video 2, an animation that fades between the two images. The fine-scale features in the white-light corona (Fig. 1a) are believed to be manifestations of the complexity of the underlying magnetic field. Although our calculations do not yet have enough resolution to resolve these spatial scales directly in the white-light corona, the magnetic field, as visualized by Q, does display similar fine-scale features (Fig. 1d). Many of the variegated, high-Q structures arise from the divergence of coronal field mappings as they approach the small-scale flux concentrations present in the photosphere. For an animation of Q at different longitudes see Supplementary Video 3. Animations that fade between an eclipse image and Q and pB are shown in Supplementary Video 4 and Supplementary Video 5. The complexity that is evident in the coronal magnetic field, and its associated topological consequences, including the presence of separatrices and quasi-separatrix layers (QSLs), has been termed the "separatrix web," or S-web[41–43]. It may provide the key to the origin of the slow solar wind, which has a distinctly different structure and composition from the fast wind. A key development of our model is to capture, self-consistently, the propagation of Alfvén waves, and the resultant coronal heating, in the backdrop of this magnetic complexity.

In addition to this comparison with eclipse observations, we compare with observations on other days to highlight interesting structures that are present in a three-dimensional model of the corona. In Figure 2 we compare predicted EUV emission on 25 July 2017 with AIA observations in the 171 Å, 193 Å, and 211 Å channels. This date falls within the range of magnetic field observations used for the prediction, one solar rotation prior to the eclipse. The predicted emission broadly matches the contrast and level

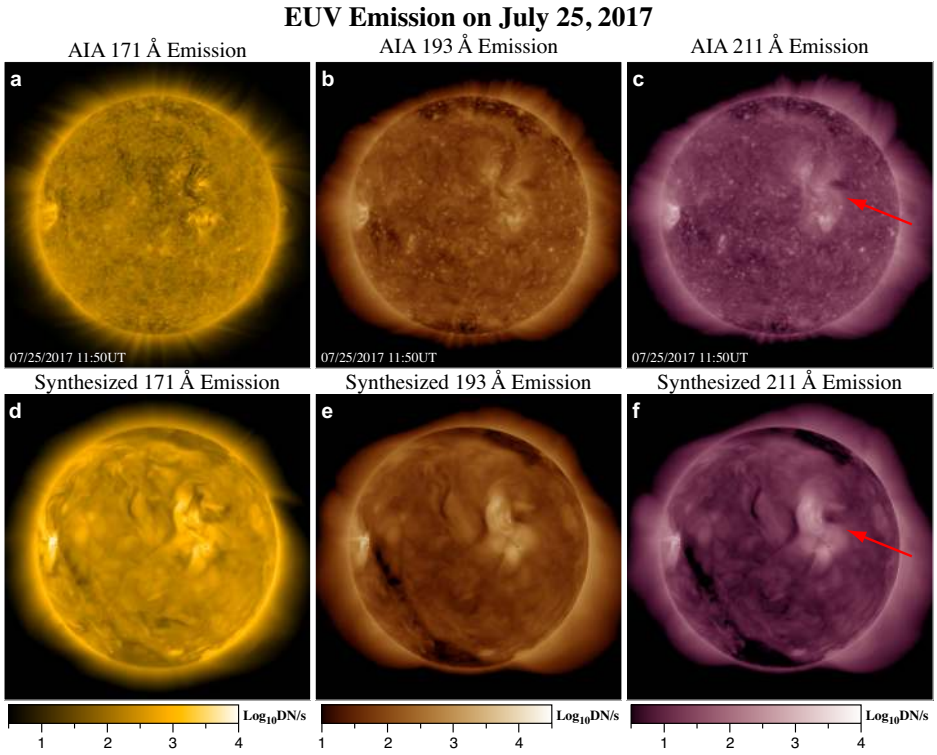

Figure 2. Comparison between observed and predicted EUV emission. Observed EUV emission (**a**, **b**, and **c**) in the 171 Å (Fe IX), 193 Å (Fe XII and XXIV), and 211 Å (Fe XIV) AIA channels, deconvolved with the point-spread function, on 25 July 2017, one solar rotation prior to the eclipse, compared with simulated emission (**d**, **e**, and **f**) from the prediction. The images are oriented with solar north up. The red arrows indicate the diffused active region with a nonpotential character.

of observed emission across a wide variety of solar features, including coronal holes, which appear as extended dark regions, and active regions, which appear bright. There also are significant differences in the details, associated with temporal changes of the corona and the limited spatial resolution of the model, so the agreement must be considered qualitative. Coronal holes are locations with largely unipolar magnetic field in the photosphere, in which the magnetic field lines are open, and are believed to be the source of the fast solar wind. At this phase of the solar cycle the polar coronal holes are ubiquitous, and sometimes extend to lower latitudes. Since the level of emission is sensitive to the amount and distribution of coronal heating, this confirms that the WTD model performs well. The diffused active region at latitude 22°N, longitude 305°, indicated by red arrows in Figure 2, shows a significant nonpotential character, a consequence of the magnetic shear introduced along the polarity inversion line (PIL) passing through it (see Supplementary Figure 5).

Unraveling the Sun's Complexity

Although the agreement between the modeled features of the large-scale corona and observations is heartening, having a sophisticated model allows us to unravel the origin of interesting structures observed during the eclipse, and to examine theories in detail. To illustrate this, we describe the interpretation of several prominent thin rays[44] seen on the east limb (on the left side of the image) at near-equatorial latitudes in Figure 1a. These extended rays resemble polar plumes. Their origin can be traced by examining an animation of volume-rendered Q from different viewpoints (Supplementary Video 6). They

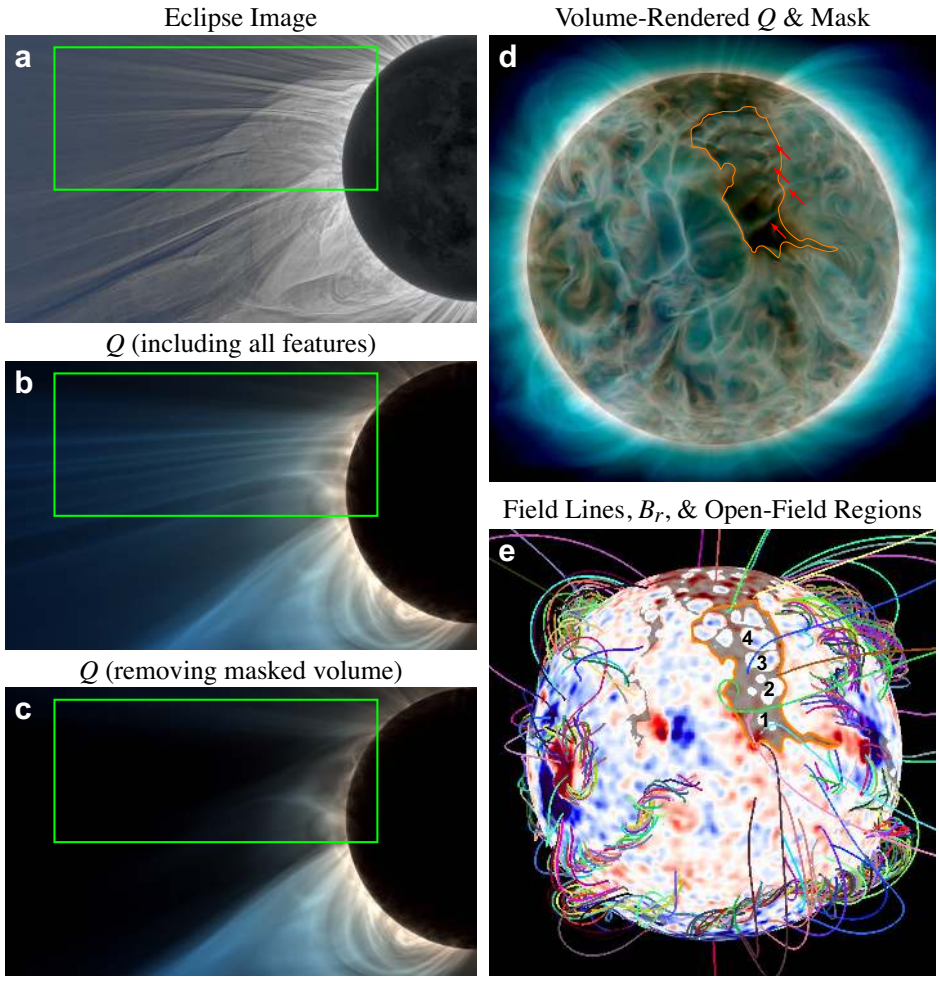

Figure 3. Investigating the origin of equatorial rays. The equatorial rays seen in the eclipse image **a** are present in the volume-rendered Q image **b** (within the green box). **c**, When the structures that connect to the low-latitude portion of the coronal hole are removed (within the volume that maps to the interior of the mask outlined in orange in **d** and **e**), the rays disappear, verifying that their source is within the coronal hole. **d**, A view of Q when the Sun is rotated by 117° about its axis to make the coronal hole visible. The red arrows point to the bases of 4 prominent rays. **e**, Open-field regions (transparent gray), B_r with blue (red) indicating negative (positive) values, and traces of magnetic field lines in arbitrary colors. The numbers 1–4 in **e** mark the parasitic polarity at the base of the rays. It is also evident from **d** and **e** that the polar plumes in the northern coronal hole emanate from locations with parasitic polarity.

are embedded in a low-latitude coronal hole that extends from the northern polar coronal hole that was located on the east limb at the time of eclipse. To illustrate this explicitly, we artificially "mask out" these features in the model, as illustrated in Figure 3. The rays are shown in a zoomed-in region of the eclipse image (Fig. 3a), together with a volume rendering of Q (Fig. 3b), and a version in which the contribution to Q from all field lines emanating from the low-latitude portion of the coronal hole has been masked out (Fig. 3c). The rays are clearly missing in Figure 3c, leaving only the curved feature of the streamer cusp, verifying that they are located in the coronal hole. A tracing of the mask in the photosphere is shown in orange in Figures 3d and 3e, with the Sun rotated to visualize the coronal hole. We conclude that the

rays are indeed similar to plumes[45], since they connect at their base to locations in coronal holes with parasitic magnetic polarity (Fig. 3e). Even though the simulated rays qualitatively resemble the observed ones, their individual brightness and locations are different. These are likely to be transient features because they are associated with small regions of parasitic polarity that cannot be captured using synoptic data.

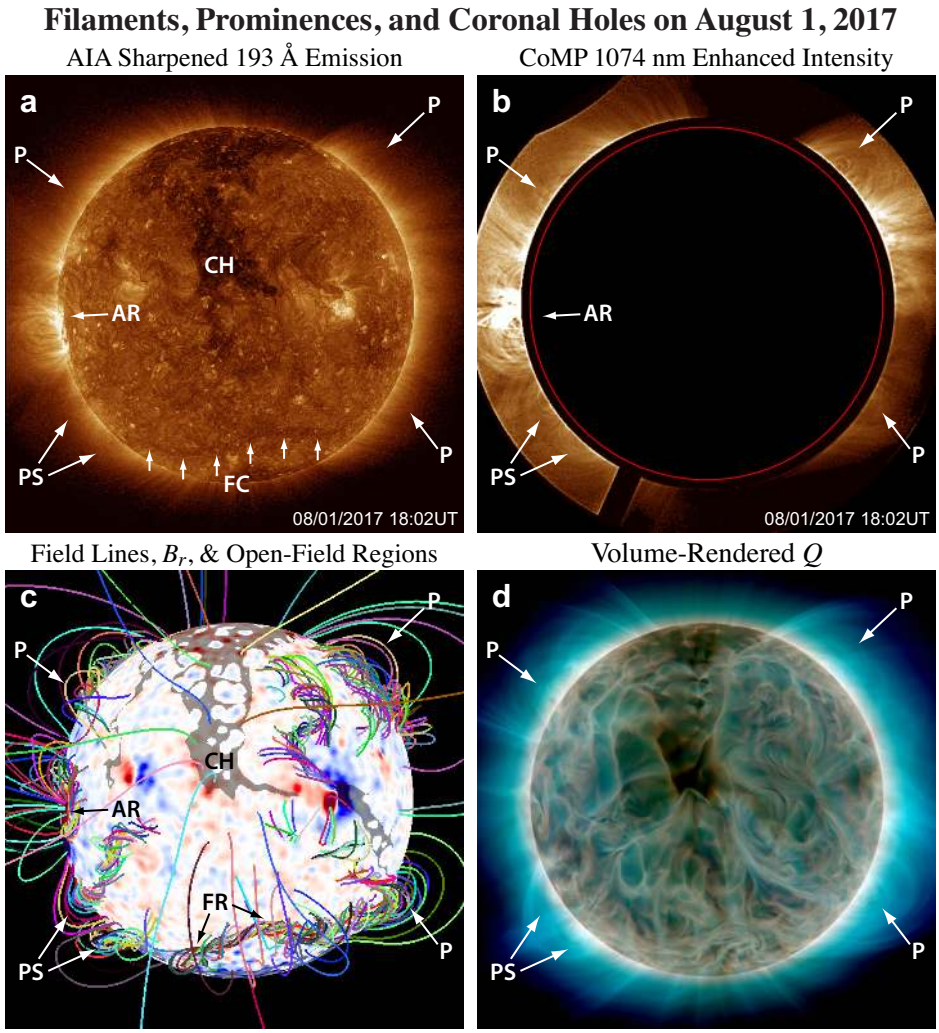

Figure 4. Comparison between observed features and model predictions. **a**, Sharpened AIA 193 Å EUV emission on 1 August 2017. **b**, Enhanced intensity of the 1074 nm Fe XIII coronal emission line from the MLSO CoMP instrument. **c**, Model predictions, including open-field regions (transparent gray), B_r with blue (red) indicating negative (positive) values, and traces of magnetic field lines in arbitrary colors. **d**, Volume-rendered squashing factor Q. Bright loops in an active region (AR) are visible on the limb (**a** and **b**). Dark coronal holes (CH) in EUV emission **a** correspond with open-field regions in the model **c**. Dark filament channels (FC) in emission **a** correspond with the location of a twisted flux rope (FR) in the model **c**. Cavities associated with prominences (P) and a pseudostreamer (PS) on the limbs in AIA and CoMP, **a** and **b**, agree with magnetic structures in the model, **c** and **d**.

Several large-scale features in EUV emission can be examined with the model. Global manifestations of twist in the coronal magnetic field are seen in filament channels that appear as narrow "dark lanes" in coronal EUV emission on the disk, indicating the presence of cooler material. At certain times these

locations are the sites of filaments, in which the coronal plasma condenses to chromospheric temperatures, which appear in Hα and in the 304 Å AIA channel. We illustrate these features in Figure 4, in which we compare observations with predictions on 1 August 2017. Figure 4a shows a 193 Å AIA image, sharpened[46] to emphasize fine details. The northern coronal hole (marked CH), which appears dark, can be seen to extend to equatorial latitudes. This area corresponds to locations with open field lines in the model (Fig. 4c), in a positive-polarity region (red), with small parasitic negative-polarity intrusions (blue). The twisted magnetic fields in a long flux rope (marked FR in Fig. 4c), correspond to a dark filament channel with the same shape in the EUV image (marked FC in Fig. 4a). Supplementary Video 9 compares the locations of energized filament channels with a synoptic map of AIA 193 Å emission.

On the limbs, prominences are associated with coronal cavities[47]. These are locations with reduced EUV emission that coincide with the flux ropes that magnetically support the cold and dense material in prominences. The 193 Å emission from AIA (Fig. 4a) and the enhanced intensity from the 1074 nm Fe XIII coronal emission line measured at Mauna Loa Solar Observatory (MLSO) with the CoMP instrument[48] (Fig. 4b) show the cavities associated with the flux ropes/prominences. A volume rendering of Q (Fig. 4d), which emphasizes the shape of magnetic structures on the limbs, shows good correspondence between the twisted flux ropes in the model that extend to the solar limbs and the cavities associated with prominences (marked P) in these images. In particular, a pseudostreamer[29] (marked PS), with two prominence cavities embedded in it, is clearly visible in AIA and CoMP on the southeast limb. The model shows the flux ropes that support these prominences in the same location (Fig. 4c), and these are clearly visible in Q (Fig. 4d). Animations of Q (Supplementary Video 6) and the magnetic field lines (Supplementary Video 7) versus longitude aid in following the 3D structure of these flux ropes.

The Missing NW Pseudostreamer

One notable disagreement between our prediction and the observed corona is the small pseudostreamer[29] that extends to large radius on the northwest limb (top center-right in Figs. 1a and 1b). The eclipse images show that it contains two prominences at its base, typical of pseudostreamers, which are associated with a double reversal (a "switchback") in the large-scale polarity inversion line (PIL)[29]. This structure is not seen in the predicted pB images (Figs. 1c and 1f), though the Q image (Fig. 1d) does show a tendency for an extended radial feature there. Careful analysis of the photospheric magnetic field synoptic chart used for the prediction (Supplementary Fig. 2) shows that the requisite PIL switchback is not present near the northwest limb (latitude 50°N, longitude 21°), precluding the formation of a pseudostreamer there. The magnetic field measurements in that neighborhood date from 16–20 July 2017, so they are over a month old by eclipse time. Newer observations, from 12–16 August 2017, show that the magnetic fields in that location are evolving, and the switchback now extends to the northwest limb (see Supplementary Figure 3), supporting the formation of a pseudostreamer. Interestingly, the SFT model correctly predicted a reversal at that location, as well as the associated pseudostreamer[19].

In Figure 5 we examine the PIL from different models at 21:52UT on August 14, 2017. This view is convenient to investigate the NW pseudostreamer because structures that were located at the west limb at eclipse time are at central meridian in this view. Fig. 5a shows photospheric B_r and the PIL (black line) for the synoptic HMI data used for our prediction (Supplementary Figure 2), compared to the PIL from the SFT model (magenta line). [The PIL from the SFT model is for the prediction[19] for 21 August 2017, obtained from their Fig. 3a]. Note that the tongue of negative polarity from the SFT model extends almost to the east limb (red arrows), and at central meridian it has the required switchback that allowed a pseudostreamer to form in the SFT model prediction[19]. The PIL in the map we used (black line), which used HMI data from July 16–August 11, does not reach central meridian (green arrows), explaining why

the NW pseudostreamer was absent in our prediction. Fig. 5b makes the same comparison, but now with updated HMI magnetic field data (July 20–August 16) corresponding to CR2193 (Supplementary Figure 3). The negative polarity (blue values) now reaches central meridian, implying that a prediction with this data would produce the NW pseudostreamer, an idea we intend to explore.

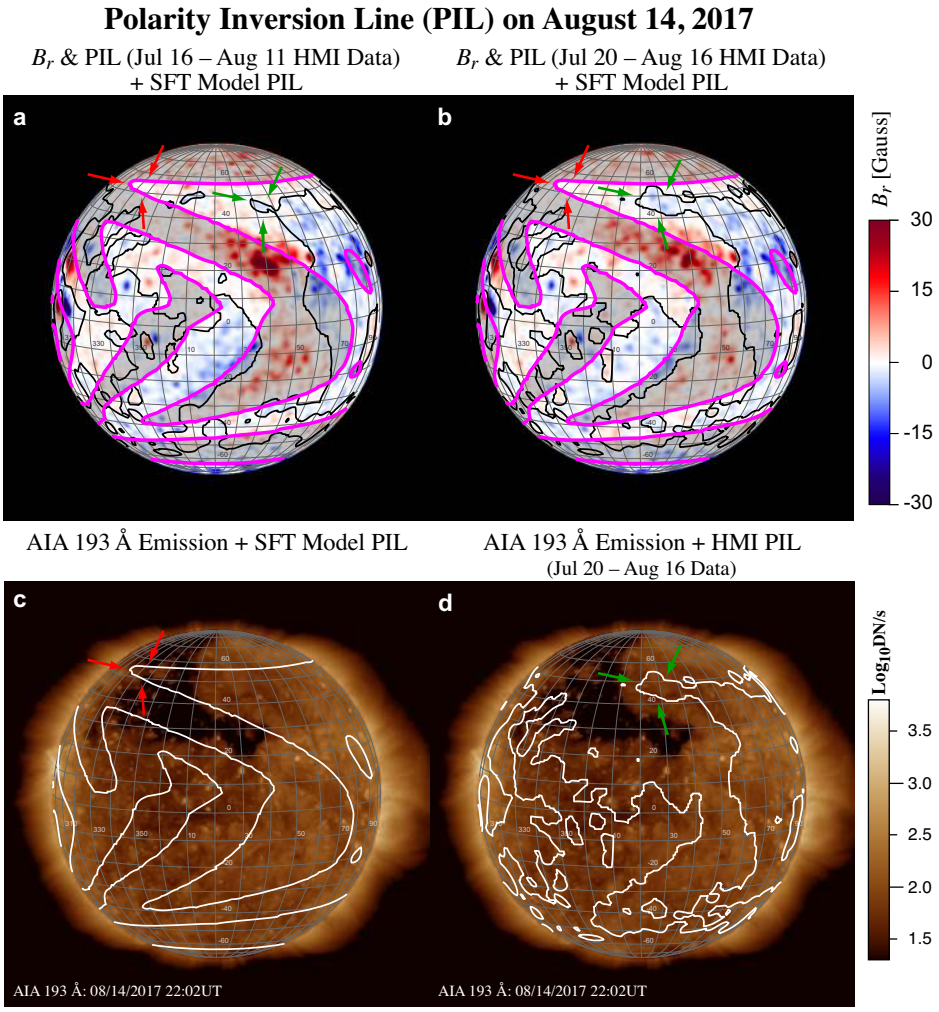

Figure 5. Polarity Inversion Line Comparison. a, B_r and the PIL (black line) from HMI data used for the prediction, compared with the PIL from the SFT model (magneta line). Positive (negative) B_r values from HMI are shown in red (blue). Positive-polarity regions in the SFT model are shaded a transparent gray. **b**, Same as **a**, but with updated HMI data (July 20–August 16). **c**, An overlay of the SFT model PIL (white line) on an AIA 193 Å EUV emission image. The extended dark region indicates a coronal hole. **d**, An overlay of the PIL from the updated HMI data on the same 193 Å image. In these views, the NW pseudostreamer that was on the west limb at eclipse time is at central meridian. The red arrows show the switchback in the SFT model PIL that allows the NW pseudostreamer to form; the green arrows show the switchback in the PIL from HMI synoptic data. These PILs are discussed in the text.

As already noted, coronal holes are unipolar regions, and therefore should not be crossed by PILs. Overlays of the PIL (white lines) from the SFT model and the updated HMI data on AIA 193 Å images are shown in Figs. 5c and 5d, respectively. A prominent coronal hole with positive polarity is seen to extend from the pole to low latitudes. It appears that the SFT model PIL (Fig. 5c) extends too far eastward:

the negative-polarity region (red arrows) encroaches into the positive-polarity coronal hole, leading to an inconsistency. On the other hand, the PIL from the updated HMI data (Fig. 5d) correctly stops short of the coronal hole boundary (green arrows).

Clearly, getting the most accurate representation of the magnetic field is of paramount importance when making predictions. As we have seen, synoptic magnetic field data, which are built up from observations from a single vantage point over a solar rotation, can lead to inaccuracies. An alternative is to use a flux-transport model that evolves the field over the whole Sun to predict the magnetic field into the future (making assumptions about the field that emerges in the intervening time). Because of the simplicity with which flux is added into the SFT model (i.e., in idealized bipolar active regions)[19], its predictions are subject to inaccuracies in active regions, and especially at lower latitudes. It has already been recognized that flux transport models that do not use data assimilation can introduce fundamental inaccuracies in high-latitude and polar fields[49]. It is likely that techniques that assimilate magnetograms into a flux transport model, such as the Schrijver & DeRosa model[50], the ADAPT model[51,52], and the Advective Flux Transport model[53], offer the best of both worlds, allowing for prediction of fields into the future while at the same time incorporating observations.

Prospects

Along with improved measurement techniques, computer models of the Sun have come of age. The sophistication of the models allows us to explore the details of coronal structures and the physics behind them. Our inability to measure the magnetic field instantaneously over the whole surface of the Sun limits the accuracy of our forecasts. Fortunately, this can be remedied by locating multiple spacecraft off the Sun-Earth line (e.g., at the L5 Lagrange point[49]). With improved data, a model such as the one we describe can be extended to track the continuous evolution of the Sun, similar to what is done in terrestrial weather models, with the potential to provide more accurate forecasts, including the initiation and propagation of coronal mass ejections. In the near term, detailed modeling will be crucial to provide the global context needed to interpret detailed measurements from the upcoming Parker Solar Probe and Solar Orbiter missions (to be launched in 2018 and 2020, respectively), which promise to give us new insight into the near-Sun environment.

Methods

Magnetohydrodynamic Model. The coronal eclipse prediction was performed using the MAS code, which solves the resistive MHD equations in spherical coordinates (r, θ, ϕ) on nonuniform meshes using a semi-implicit time-stepping algorithm. The method of solution, including the boundary conditions, has been described previously[54–58]. The model simulates the global corona and solar wind out to $15R_\odot$ and beyond[20,21,59,60]. A primary application of MAS is to simulate realistic magnetic configurations that are observed in the corona, which is achieved by using observational measurements of the radial component of the photospheric magnetic field, B_r, as a primary boundary condition. In this case, we used synoptic observations taken with the HMI magnetograph[23,61] aboard the SDO spacecraft[24] to specify B_r. The model includes a sophisticated treatment of the flow of energy, including thermal conduction along the magnetic field, optically thin radiative losses, and an advanced treatment of coronal heating[20,57,62], allowing the plasma density, temperature, and velocity to be computed in addition to the magnetic field. With this information we can accurately estimate EUV and soft X-ray emission that are observed from space[21,22,63], as well as white-light polarized brightness, which is best seen during eclipses, but can also be measured from the ground and in space.

Developing a model of the corona involves specifying parameters, including the Alfvén wave flux in the WTD model, the possible scaling of the photospheric magnetic field, and the abundance of elements in the corona. In general, the values of these parameters can be constrained by multiple observations, including EUV emission from AIA and spectrographs, scattered white light from coronagraphs, and additional observations that depend on the coronal magnetic field, such as radio emission, Faraday rotation, and the intensity in infrared spectral lines, and *in situ* measurements of plasma properties, magnetic fields, and charge states in the solar wind, among others. Comprehensive assimilation of these measurements into a model is a complex endeavor that is still in its infancy. We used an *ad hoc* procedure to constrain our parameters by considering a subset of these diagnostics. In the months leading up to the eclipse, we ran a series of 17 medium-resolution simulations (with $204 \times 148 \times 315$ mesh points) using the HMI B_r synoptic map for CR 2189 (2–29 April 2017). We made the following comparisons: 1) simulated EUV images were compared with AIA observations at three different periods during the rotation; 2) the size and morphology of coronal holes deduced from synoptic maps of observed AIA EUV emission[64] were compared with open-field boundaries from the model[65]; 3) the off-limb differential emission measure (DEM)-weighted temperature, deduced from fits to AIA emission[66], was compared with a similarly deduced temperature from the model; 4) simulated white-light polarized brightness and the morphology of streamers were compared with MLSO K-Cor coronagraph data[67]. We used these comparisons to fine-tune the heating in the model, expressed as the flux of Alfvén waves at the base of the corona. We eventually found a reasonable (though not perfect) agreement with all four diagnostics. This idea is summarized visually in Supplementary Figure 1, which compares the final prediction with some of these diagnostics on 25 July 2017, one solar rotation prior to the eclipse.

An important choice in our model was to specify the abundances of elements in the corona, which are not known precisely. For the final prediction we used coronal abundances, in conjunction with the CHIANTI 7.1[68] radiative loss function. For consistency, we used identical abundances to synthesize EUV emission. An alternate popular choice is to use photospheric abundances, which are generally lower. During our experiments, we found that, to zero order, changing the abundances in this way does not produce widely different coronal EUV emission, but it does affect the predicted plasma density in the corona (in a ratio that is inversely proportional to the square root of the abundances). From Supplementary Figure 1 it is apparent that our predicted pB is less bright than that inferred from MLSO K-Cor. Quantitatively, the predicted values are about a factor of 2 smaller. Since pB is proportional to plasma density, we could

have chosen to increase pB in our model by using photospheric abundances. This issue will be examined further in the future, possibly by comparing with other eclipse measurements.

Our final prediction was performed in two phases: a preliminary prediction, three weeks before the eclipse, and a final prediction, with updated magnetic field observations, one week prior to the eclipse, which was posted on our website (http://predsci.com/eclipse2017) on 15 August 2017. The timing of the synoptic magnetic field data we used is described in the main article. The high-latitude fields were fit using the procedure described in Supplementary Note 1. We multiplied the B_r inferred from HMI by the factor of 1.4 to account for the difference in magnetic field strengths measured by the HMI magnetograph and its predecessor, the MDI magnetograph on SOHO[69], since several of our previous eclipse predictions used MDI data, and our model parameters were benchmarked to MDI data. In general, photospheric magnetic fields measured by different instruments are qualitatively similar but differ quantitatively[70], and the true values are unknown[65]. Thankfully, the increase of B_r by this factor is not an essential aspect of the model. Similar results could be obtained by leaving B_r unchanged and using a different driving amplitude for Alfvén waves in the photosphere. The proper scaling of B_r must await confirmation by more reliable observations. Supplementary Figure 2 shows the photospheric radial magnetic field that was used in the calculation. Magnetic field data for CR 2193, which has updated measurements from 12–16 August 2017 at the location of the eclipse-day west limb (longitudes 0°–51°), is shown in Supplementary Figure 3. This updated data relates to the inaccuracy in the prediction of the observed northwest pseudostreamer, as discussed in the Prospects section of the main article.

The simulation used a high-resolution mesh, with $295 \times 315 \times 699$ (r, θ, ϕ) mesh points, with a uniform angular resolution of 0.52° in longitude (corresponding to 6,300 km at the Sun's surface), and a similar latitudinal resolution at the equator that increased to 1.23° towards the poles. The radial resolution was finer in the transition region ($\Delta r = 260$ km) to resolve the thermal conduction length-scale at low heights (which is artificially broadened using a special, solution-preserving technique[21,71]), and grows to match the horizontal resolution with radius, maximizing at $\Delta r = 290{,}000$ km at the upper boundary, $r = 15 R_\odot$.

The calculation for the final prediction was run on 4,200 Pleiades CPU cores at NASA's Advanced Supercomputing facility. The first run simulated the relaxation of the corona for 60 hours of solar time (solution A), starting from the final state of a previous run (the preliminary prediction from 31 July, with magnetic fields updated to 8 August). A separate zero-beta simulation, in which the magnetic field was energized, was performed at the same time (solution B). The energization procedure is described below. The final magnetic field in this energized solution had the same B_r at $r = R_\odot$ as that in solution A. A third and final run then updated solution A with the nonpotential component of the magnetic field from solution B[72], relaxing the corona for an additional 8 hours to equilibrate the energized field with the large-scale corona from solution A. This end-state was used to produce the quantities for the prediction.

Coronal Heating Model. The heating of the corona was specified by using a wave-turbulence-driven (WTD) phenomenology to advance equations for Alfvén wave amplitudes along with the MHD equations. Our model is based on the idea that the interaction of outward and reflected waves is responsible for the dissipation of the waves, producing coronal heating[28]. This follows related works, where the general formalism for the propagation of Alfvén waves[73–75] is usually approximated to produce tractable equations for their propagation[28,76–86]. Our approach advances the amplitudes of the waves, rather than the energy densities, in terms of the Elsasser variables $\mathbf{z}_\pm = \delta\mathbf{v} \mp \delta\mathbf{B}/\sqrt{4\pi\rho}$, where $\delta\mathbf{v}$ and $\delta\mathbf{B}$ are the perturbed wave quantities. For incompressible transverse waves that are isotropic about the direction of the mean magnetic field, $\mathbf{B}$, the vector quantities $\mathbf{z}_\pm$ reduce to the scalar complex Fourier amplitudes z_+ and z_- for a wave with frequency ω. The amplitudes z_+ and z_- represent outward and inward propagating waves

along an open field line directed away from the Sun. Starting from equations for the evolution of z_+ and z_-, we take the zero-frequency limit of these equations to describe the propagation of low-frequency Alfvén waves, for which z_+ and z_- become real scalar quantities[79,87,88]. The following equations are advanced in MAS:

$$\frac{\partial z_\pm}{\partial t} + (\mathbf{v} \pm \mathbf{v}_A) \cdot \nabla z_\pm = R_1 z_\pm + R_2 z_\mp - \frac{|z_\mp| z_\pm}{2\lambda_\perp}, \tag{1}$$

$$R_1 = \frac{1}{4}(\mathbf{v} \mp \mathbf{v}_A) \cdot \nabla(\log \rho), \qquad R_2 = \frac{1}{2}(\mathbf{v} \mp \mathbf{v}_A) \cdot \nabla(\log |\mathbf{v}_A|), \tag{2}$$

where R_1 and R_2 are the diagonal (WKB) and off-diagonal (non-WKB) terms, respectively, and $\mathbf{v}_A$ is the Alfvén velocity. The self-reflection term, R_2, allows for the conversion of an outgoing wave into an incoming wave (and vice versa)—a crucial effect that is not captured in the WKB approximation. The last term in Equation (1) is a phenomenological wave dissipation term[89–93] that produces a volumetric heating rate in the energy equation,

$$H_{\mathrm{WTD}} = \rho \frac{|z_-| z_+^2 + |z_+| z_-^2}{4\lambda_\perp}, \tag{3}$$

where $\lambda_\perp$ is the transverse correlation scale that varies with the flux tube area, $\lambda_\perp = \lambda_0 \sqrt{B_0/B}$, where λ_0 and B_0 are set to typical values at the solar surface. The waves accelerate the solar wind via the wave pressure, $p_w = \rho(z_- - z_+)^2/8$, that feeds into the MHD momentum equation[25,26].

This formalism provides a minimal description of coronal heating that is physically motivated, including a self-consistent treatment of the reflection and dissipation of Alfvén waves. The free parameters are the amplitude of waves at the inner boundary, z_0, and the factor $\lambda_0 \sqrt{B_0}$. Before implementing the WTD formulation into MAS we explored it extensively using a 1D hydrodynamic code, to gain intuition for parameter choices and the scaling of the model, and to ensure that it would be suitable for multi-dimensional MHD modeling. Our work has demonstrated the scaling and applicability of the WTD model to both open-field regions, where the solar wind is accelerated[25,26], and closed-field regions[27], where the corona is heated to several million degrees. The heating adapts automatically to local conditions, changing from low values with long scale lengths in open-field regions to large heating with short scale lengths in closed-field regions[27]. This ability for the model to adapt to both open- and closed-field regions without the need to track the open/closed field boundary makes it particularly suitable for 3D MHD models, where field-line connectivity changes in time.

To provide a visual sense for the overall heating and its variation in space, we show an equivalent heat flux map in Supplementary Figure 4. This map is generated by radially integrating the volumetric heating rate at every location on the surface of the Sun. The net heat flux deposited along a field line is directly related to the net Poynting flux of waves entering and leaving the domain at the inner boundary[27], but the radial integration gives a better sense of where it is actually deposited in the corona.

The WTD formalism and similar approaches[85] were developed by heuristically adapting the physics from one-dimensional models to three dimensions, so it is not surprising that they misbehave in certain situations. We have found that for realistic 3D magnetic fields, some regions, such as magnetic nulls or open field lines connected to weak-field regions, may not receive enough heating in the WTD model. Moreover, the wave-pressure force may develop unphysical behavior at these locations. In the future, these limitations will be improved as we gain more experience in using the WTD model. In the meantime, for this simulation we circumvented these problems by using the wave pressure from the WKB model[21], rather than that from the WTD model, in the MHD momentum equation, and we

added two small spherically symmetric heating terms of the form $H = H_0 \exp(-(r - R_\odot)/\lambda)$ to the coronal heating from the WTD model. The first term sets a minimum heating in the transition region and low corona ($H_0 = 2.7 \times 10^{-5}$ erg/cm^3/s, $\lambda = 21$ Mm), while the second ensures a minimum heating in open-field regions ($H_0 = 2.9 \times 10^{-8}$ erg/cm^3/s, $\lambda = 696$ Mm). These terms add equivalent heat fluxes of 5.9×10^4 erg/cm^2/s and 1.0×10^4 erg/cm^2/s respectively, which are considerably smaller than the average heat flux supplied by the WTD model, which is in the range $\sim 10^5$–10^7 erg/cm^2/s (Supplementary Figure 4).

Magnetic Field Energization. Filament channels are an observable signature of nonpotential magnetic fields in the low corona. These are regions along polarity inversion lines (PILs) in the photosphere, $B_r = 0$, where the magnetic field tends to be highly sheared, lying almost parallel to the PILs[32]. These filament channels are especially prevalent during this declining phase of the solar cycle, when the strong magnetic fields in active regions are confined to a limited number of locations. They consist of long, low-lying structures that sometimes have filament/prominence material that is visible in Hα and He 304 Å[94]. On occasion they erupt spectacularly. During the 21 August 2017 eclipse, a prominence was seen to erupt on the southeast limb in AIA images just before the eclipse. Quiescent prominences were seen on the west limb at the base of coronal streamers during the eclipse (appearing reddish in the white-light images, as seen in Figure 1). In order to capture these structures in our prediction we emerged sheared magnetic fields in these filament channels in our model, to "energize" the corona. The energization procedure is described in the section on the MAS model by Yeates et al.[95] The PIL at a height $r = 1.05R_\odot$ was determined from the initial potential field. Segments of this PIL were selected for energization according to the presence of filament channels, determined by examining movies of EUV emission from the AIA instrument on SDO during the period 16 July–12 August 2017, in the 171 Å, 193 Å, and 211 Å channels, enhanced to emphasize filament channels[46]. Additional flux, ΔB_r, was added in the neighborhood of these segments; this flux is later cancelled in the final phase of the energization. The flux was added in channels that were $\sim 0.1R_\odot$ wide, and amounted to between 10% and 30% of the existing flux in these channels. Transverse magnetic field, $\mathbf{B}_t$, was emerged along these segments, parallel to the PIL, by applying a transverse electric field $\mathbf{E}_t = \nabla_t \Phi$ at $r = R_\odot$, where ∇_t is the transverse gradient, with $\Phi = MB_r$, where M is a mask that localizes $\mathbf{B}_t$ to a neighborhood of the PIL.

The chirality of the magnetic field in filament channels (i.e., the direction of the transverse field along the PIL) was determined by running a separate calculation using a flux transport model, combined with the magnetofrictional model[34,96–98]. We simulated the nonpotential Sun continuously from 1 January–29 July 2017, by adding the active regions that were observed to emerge in HMI magnetograms, as assimilated into the Advective Flux Transport model[53]. This simulation was used to specify the direction of the emerged $\mathbf{B}_t$ in the MHD model by choosing the appropriate sign of M.

This process introduced a highly sheared magnetic field in the filament channels. Supplementary Figure 5 shows the location of the filament channels that were energized, as well as the potential Φ. This emergence phase was followed by a flux cancellation phase, in which the added flux, ΔB_r, was cancelled, by applying a transverse electric field $\mathbf{E}_t = \nabla_t \times \Psi \hat{\mathbf{r}}$ at $r = R_\odot$, with Ψ determined from $\nabla_t^2 \Psi = \Delta B_r / \Delta T$, where ΔT is the time interval over which $\mathbf{E}_t$ is applied. This cancellation tends to reconnect sheared magnetic fields, producing flux-rope-like structures, raising them slightly into the corona in the process. At the end of this phase the radial magnetic field B_r at $r = R_\odot$ matches the observed field. The correspondence between the location of the energized filament channels and those inferred from a synoptic map of observed emission in AIA 193 Å [data supplied by Nishu Karna[99]] can be seen in Supplementary Video 9, an animation that fades the energized channels on a background image of the synoptic emission. Supplementary Figure 6 shows a comparison of the corona before and after energiza-

tion, visualized by a volume rendering of the squashing factor Q, showing that the sheared magnetic fields inflate the streamers and pseudostreamers with flux ropes, with an appearance that resembles prominence cavities. Supplementary Video 8 shows a fade of Q between the unenergized and energized corona.

Squashing Factor of Magnetic Flux Tubes. To illustrate the complexity of the eclipse corona we developed a novel way to visualize the magnetic field structure using a composite, line-of-sight (LOS) rendering of the squashing factor[38,100]. The squashing factor, Q, is a geometric characteristic of the magnetic field line mapping from one boundary to another. Conceptually it expresses how much an infinitesimal circle on one boundary is "squashed" into an ellipse as it is mapped along magnetic field lines to the other boundary[38]. Q becomes very large or infinite at locations where the magnetic structure experiences abrupt variation[101–103].

Visualizing the information contained in a 3D Q mapping is challenging, requiring the tracing of billions of magnetic field lines. It can be divided into two steps: the computation of Q, and the ensuing visualization of this quantity. We compute Q by exploiting the fact that it has the same value along a field line. We first compute Q at high resolution on the inner and outer radial spherical boundaries (at $4\times$ the resolution of the computation grid, using 16 points per simulation mesh point). The value of Q at each point in the 3D volume is obtained by tracing field lines from the point, in both directions, to their intersections with the inner and outer spherical boundaries, interpolating Q at these locations using cubic spline interpolation, and averaging the two values. We computed Q at 520 million locations inside the 3D volume, on a mesh that is $2\times$ the resolution (in each dimension) of the computation volume. To visualize the 3D Q mapping, we render color images in the plane of the sky, which are then animated with solar rotation to aid in the 3D visualization of Q. The three color channels of each image, red (R), blue (B), and green (G), each contain position-weighted integrals of $\log_{10} Q$ along the LOS, at each pixel, which are combined into a color RGB image. The R, G, and B color channels use different spatial weightings to give a sense of "depth" to the visualized Q, as described in Supplementary Note 2.

Eclipse Observations. The Williams College Eclipse Expedition observed from the campus of Willamette University, in Salem, Oregon. The images used in the composite were taken with Nikon 400-mm and 800-mm lenses and Nikon D810 cameras controlled by the program Solar Eclipse Maestro (from Xavier Jubier). The images were assembled digitally, using a group of custom manual techniques to stack, merge, correct, and optimize them into a composite image that closely approaches the naked-eye appearance of the corona, within the limits of the medium.

Code availability. We have opted not to make the MAS code available at the present time because of the complexity involved in its use, and the expertise required to run it. The support that we would need to provide to users exceeds our current resources. A version of MAS is available for "runs on demand" at NASA's Community Coordinated Modeling Center (CCMC), at https://ccmc.gsfc.nasa.gov.

Data availability. The magnetic field data from the HMI instrument and the EUV data from the AIA instrument on SDO are publicly available at the Joint Science Operations Center (JSOC). The data from the Mauna Loa Solar Observatory (MLSO) are publicly available at their web site. The eclipse images are included in this published article. Some of the other images are publicly available at the Predictive Science, Inc. web site, http://predsci.com/eclipse2017. The other datasets generated during the current study are available from the corresponding author on reasonable request.

References

1. Pasachoff, J. M. Solar eclipses as an astrophysical laboratory. *Nature* **459**, 789–795 (2009). DOI 10.1038/nature07987.

2. Habbal, S. R., Morgan, H. & Druckmüller, M. Exploring the Prominence-Corona Connection and its Expansion into the Outer Corona Using Total Solar Eclipse Observations. *Astrophys. J.* **793**, 119 (2014). DOI 10.1088/0004-637X/793/2/119.

3. Pasachoff, J. M. Astrophysics: The great solar eclipse of 2017. *Scientific American* **317**, 54–61 (2017). DOI http://dx.doi.org/10.1038/scientificamerican0817-54.

4. Parnell, C. E. & De Moortel, I. A contemporary view of coronal heating. *Philosophical Transactions of the Royal Society of London A* **370**, 3217–3240 (2012). DOI 10.1098/rsta.2012.0113.

5. Priest, E. *Magnetohydrodynamics of the Sun* (Cambridge University Press, 2014).

6. Klimchuk, J. A. Key aspects of coronal heating. *Philosophical Transactions of the Royal Society of London Series A* **373**, 20140256–20140256 (2015). DOI 10.1098/rsta.2014.0256.

7. Amari, T., Canou, A., Aly, J.-J., Delyon, F. & Alauzet, F. Magnetic cage and rope as the key for solar eruptions. *Nature* **554**, 211–215 (2018). DOI 10.1038/nature24671.

8. Vivès, S., Lamy, P., Koutchmy, S. & Arnaud, J. ASPIICS, a giant externally occulted coronagraph for the PROBA-3 formation flying mission. *Advances in Space Research* **43**, 1007–1012 (2009). DOI 10.1016/j.asr.2008.10.026.

9. Habbal, S. R. *et al.* Mapping the Distribution of Electron Temperature and Fe Charge States in the Corona with Total Solar Eclipse Observations. *Astrophys. J.* **708**, 1650–1662 (2010). DOI 10.1088/0004-637X/708/2/1650.

10. Habbal, S. R. *et al.* Thermodynamics of the Solar Corona and Evolution of the Solar Magnetic Field as Inferred from the Total Solar Eclipse Observations of 2010 July 11. *Astrophys. J.* **734**, 120 (2011). DOI 10.1088/0004-637X/734/2/120.

11. Pasachoff, J. M. Heliophysics at total solar eclipses. *Nature Astronomy* **1**, 0190 (2017). DOI 10.1038/s41550-017-0190.

12. Dyson, F. W., Eddington, A. S. & Davidson, C. A Determination of the Deflection of Light by the Sun's Gravitational Field, from Observations Made at the Total Eclipse of May 29, 1919. *Philosophical Transactions of the Royal Society of London Series A* **220**, 291–333 (1920). DOI 10.1098/rsta.1920.0009.

13. Hawking, S. *A Brief History of Time: From the Big Bang to Black Holes* (Bantam Books, 1988).

14. Kennefick, D. Testing relativity from the 1919 eclipse—a question of bias. *Physics Today* **62**, 37 (2009). DOI 10.1063/1.3099578.

15. Schindler, S. Theory-laden experimentation. *Studies in History and Philosophy of Science Part A* **44**, 89–101 (2013).

16. Mikić, Z., Linker, J. A., Riley, P. & Lionello, R. Predicting the Structure of the Solar Corona During the 11 August 1999 Total Solar Eclipse. In Livingston, W. & Özgüç, A. (eds.) *Last Total Solar Eclipse of the Millennium*, vol. 205 of *Astronomical Society of the Pacific Conference Series*, 162 (2000).

17. Mikić, Z., Linker, J. A., Lionello, R., Riley, P. & Titov, V. Predicting the Structure of the Solar Corona for the Total Solar Eclipse of March 29, 2006. In Demircan, O., Selam, S. O. & Albayrak, B. (eds.) *Solar and Stellar Physics Through Eclipses*, vol. 370 of *Astronomical Society of the Pacific Conference Series*, 299 (2007).

18. Rušin, V. *et al.* Comparing eclipse observations of the 2008 August 1 solar corona with an MHD model prediction. *Astron. Astrophys.* **513**, A45 (2010). DOI 10.1051/0004-6361/200912778.

19. Nandy, D. *et al.* The Large-scale Coronal Structure of the 2017 August 21 Great American Eclipse: An Assessment of Solar Surface Flux Transport Model Enabled Predictions and Observations. *Astrophys. J.* **853**, 72 (2018). DOI 10.3847/1538-4357/aaa1eb.

20. Mikić, Z., Linker, J. A., Schnack, D. D., Lionello, R. & Tarditi, A. Magnetohydrodynamic modeling of the global solar corona. *Physics of Plasmas* **6**, 2217–2224 (1999). DOI 10.1063/1.873474.

21. Lionello, R., Linker, J. A. & Mikić, Z. Multispectral Emission of the Sun during the First Whole Sun Month: Magnetohydrodynamic Simulations. *Astrophys. J.* **690**, 902–912 (2009). DOI 10.1088/0004-637X/690/1/902.

22. Downs, C. *et al.* Probing the Solar Magnetic Field with a Sun-Grazing Comet. *Science* **340**, 1196–1199 (2013). DOI 10.1126/science.1236550.

23. Scherrer, P. H. *et al.* The Helioseismic and Magnetic Imager (HMI) Investigation for the Solar Dynamics Observatory (SDO). *Sol. Phys.* **275**, 207–227 (2012). DOI 10.1007/s11207-011-9834-2.

24. Pesnell, W. D., Thompson, B. J. & Chamberlin, P. C. The Solar Dynamics Observatory (SDO). *Sol. Phys.* **275**, 3–15 (2012). DOI 10.1007/s11207-011-9841-3.

25. Lionello, R. *et al.* Validating a Time-dependent Turbulence-driven Model of the Solar Wind. *Astrophys. J.* **784**, 120 (2014). DOI 10.1088/0004-637X/784/2/120.

26. Lionello, R., Velli, M., Downs, C., Linker, J. A. & Mikić, Z. Application of a Solar Wind Model Driven by Turbulence Dissipation to a 2D Magnetic Field Configuration. *Astrophys. J.* **796**, 111 (2014). DOI 10.1088/0004-637X/796/2/111.

27. Downs, C., Lionello, R., Mikić, Z., Linker, J. A. & Velli, M. Closed-Field Coronal Heating Driven by Wave Turbulence. *Astrophys. J.* **832**, 180 (2016). DOI 10.3847/0004-637X/832/2/180.

28. Matthaeus, W. H., Zank, G. P., Oughton, S., Mullan, D. J. & Dmitruk, P. Coronal Heating by Magnetohydrodynamic Turbulence Driven by Reflected Low-Frequency Waves. *Astrophys. J.* **523**, L93–L96 (1999). DOI 10.1086/312259.

29. Wang, Y.-M., Sheeley, N. R., Jr. & Rich, N. B. Coronal Pseudostreamers. *Astrophys. J.* **658**, 1340–1348 (2007). DOI 10.1086/511416.

30. Martin, S. F. Conditions for the Formation and Maintenance of Filaments (Invited Review). *Sol. Phys.* **182**, 107–137 (1998). DOI 10.1023/A:1005026814076.

31. Mackay, D. H., Gaizauskas, V. & Yeates, A. R. Where Do Solar Filaments Form?: Consequences for Theoretical Models. *Sol. Phys.* **248**, 51–65 (2008). DOI 10.1007/s11207-008-9127-6.

32. Mackay, D. H., Karpen, J. T., Ballester, J. L., Schmieder, B. & Aulanier, G. Physics of Solar Prominences: II—Magnetic Structure and Dynamics. *Space Sci. Rev.* **151**, 333–399 (2010). DOI 10.1007/s11214-010-9628-0.

33. Lemen, J. R. *et al.* The Atmospheric Imaging Assembly (AIA) on the Solar Dynamics Observatory (SDO). *Sol. Phys.* **275**, 17–40 (2012). DOI 10.1007/s11207-011-9776-8.

34. Yeates, A. R. Coronal Magnetic Field Evolution from 1996 to 2012: Continuous Non-potential Simulations. *Sol. Phys.* **289**, 631–648 (2014). DOI 10.1007/s11207-013-0301-0.

35. Billings, D. E. *A Guide to the Solar Corona* (New York: Academic Press, 1966).

36. Golub, L. & Pasachoff, J. M. *The Solar Corona* (Cambridge University Press, 2nd Edition, 2010).

37. Mok, Y., Mikić, Z., Lionello, R., Downs, C. & Linker, J. A. A Three-dimensional Model of Active Region 7986: Comparison of Simulations with Observations. *Astrophys. J.* **817**, 15 (2016). DOI 10.3847/0004-637X/817/1/15.

38. Titov, V. S. Generalized Squashing Factors for Covariant Description of Magnetic Connectivity in the Solar Corona. *Astrophys. J.* **660**, 863–873 (2007). DOI 10.1086/512671.

39. Druckmüller, M. A Noise Adaptive Fuzzy Equalization Method for Processing Solar Extreme Ultraviolet Images. *Astrophys. J. Suppl.* **207**, 25 (2013). DOI 10.1088/0067-0049/207/2/25.

40. Newkirk, G., Jr., Dupree, R. G. & Schmahl, E. J. Magnetic Fields and the Structure of the Solar Corona. II: Observations of the 12 November 1966 Solar Corona. *Sol. Phys.* **15**, 15–39 (1970). DOI 10.1007/BF00149469.

41. Titov, V. S., Mikić, Z., Linker, J. A., Lionello, R. & Antiochos, S. K. Magnetic Topology of Coronal Hole Linkages. *Astrophys. J.* **731**, 111 (2011). DOI 10.1088/0004-637X/731/2/111.

42. Antiochos, S. K., Mikić, Z., Titov, V. S., Lionello, R. & Linker, J. A. A Model for the Sources of the Slow Solar Wind. *Astrophys. J.* **731**, 112 (2011). DOI 10.1088/0004-637X/731/2/112.

43. Linker, J. A., Lionello, R., Mikić, Z., Titov, V. S. & Antiochos, S. K. The Evolution of Open Magnetic Flux Driven by Photospheric Dynamics. *Astrophys. J.* **731**, 110 (2011). DOI 10.1088/0004-637X/731/2/110.

44. Wang, Y.-M. *et al.* The Solar Eclipse of 2006 and the Origin of Raylike Features in the White-Light Corona. *Astrophys. J.* **660**, 882–892 (2007). DOI 10.1086/512480.

45. Pasachoff, J. M. *et al.* Polar Plume Brightening During the 2006 March 29 Total Eclipse. *Astrophys. J.* **682**, 638–643 (2008). DOI 10.1086/588020.

46. Morgan, H. & Druckmüller, M. Multi-Scale Gaussian Normalization for Solar Image Processing. *Sol. Phys.* **289**, 2945–2955 (2014). DOI 10.1007/s11207-014-0523-9.

47. Gibson, S. Coronal Cavities: Observations and Implications for the Magnetic Environment of Prominences. In Vial, J.-C. & Engvold, O. (eds.) *Solar Prominences*, vol. 415 of *Astrophysics and Space Science Library*, 323–353 (2015). DOI 10.1007/978-3-319-10416-4_13.

48. Tomczyk, S. *et al.* An Instrument to Measure Coronal Emission Line Polarization. *Sol. Phys.* **247**, 411–428 (2008). DOI 10.1007/s11207-007-9103-6.

49. Mackay, D. H., Yeates, A. R. & Bocquet, F.-X. Impact of an L5 Magnetograph on Nonpotential Solar Global Magnetic Field Modeling. *Astrophys. J.* **825**, 131 (2016). DOI 10.3847/0004-637X/825/2/131.

50. Schrijver, C. J. & De Rosa, M. L. Photospheric and heliospheric magnetic fields. *Sol. Phys.* **212**, 165–200 (2003). DOI 10.1023/A:1022908504100.

51. Arge, C. N. *et al.* Air Force Data Assimilative Photospheric Flux Transport (ADAPT) Model. *Twelfth International Solar Wind Conference* **1216**, 343–346 (2010). DOI 10.1063/1.3395870.

52. Hickmann, K. S., Godinez, H. C., Henney, C. J. & Arge, C. N. Data Assimilation in the ADAPT Photospheric Flux Transport Model. *Sol. Phys.* **290**, 1105–1118 (2015). DOI 10.1007/s11207-015-0666-3. 1410.6185.

53. Upton, L. & Hathaway, D. H. Predicting the Sun's Polar Magnetic Fields with a Surface Flux Transport Model. *Astrophys. J.* **780**, 5 (2014). DOI 10.1088/0004-637X/780/1/5.

54. Mikić, Z. & Linker, J. A. Disruption of Coronal Magnetic Field Arcades. *Astrophys. J.* **430**, 898–912 (1994).

55. Lionello, R., Mikić, Z. & Schnack, D. D. Magnetohydrodynamics of Solar Coronal Plasmas in Cylindrical Geometry. *Journal of Computational Physics* **140**, 1–30 (1998).

56. Lionello, R., Mikić, Z. & Linker, J. A. Stability of Algorithms for Waves with Large Flows. *Journal of Computational Physics* **152**, 346–358 (1999).

57. Lionello, R., Linker, J. A. & Mikić, Z. Including the Transition Region in Models of the Large-Scale Solar Corona. *Astrophys. J.* **546**, 542–551 (2001).

58. Caplan, R. M., Mikić, Z., Linker, J. A. & Lionello, R. Advancing parabolic operators in thermodynamic MHD models: Explicit super time-stepping versus implicit schemes with Krylov solvers. In *Journal of Physics Conference Series*, vol. 837 of *Journal of Physics Conference Series*, 012016 (2017). DOI 10.1088/1742-6596/837/1/012016.

59. Riley, P. *et al.* Global MHD Modeling of the Solar Corona and Inner Heliosphere for the Whole Heliosphere Interval. *Sol. Phys.* **274**, 361–377 (2011). DOI 10.1007/s11207-010-9698-x.

60. Lionello, R. *et al.* Magnetohydrodynamic Simulations of Interplanetary Coronal Mass Ejections. *Astrophys. J.* **777**, 76 (2013). DOI 10.1088/0004-637X/777/1/76.

61. Schou, J. *et al.* Design and Ground Calibration of the Helioseismic and Magnetic Imager (HMI) Instrument on the Solar Dynamics Observatory (SDO). *Sol. Phys.* **275**, 229–259 (2012). DOI 10.1007/s11207-011-9842-2.

62. Lionello, R., Mikić, Z., Linker, J. A. & Amari, T. Magnetic Field Topology in Prominences. *Astrophys. J.* **581**, 718–725 (2002). DOI 10.1086/344222.

63. Downs, C. *et al.* Toward a Realistic Thermodynamic Magnetohydrodynamic Model of the Global Solar Corona. *Astrophys. J.* **712**, 1219–1231 (2010). DOI 10.1088/0004-637X/712/2/1219.

64. Caplan, R. M., Downs, C. & Linker, J. A. Synchronic Coronal Hole Mapping Using Multi-instrument EUV Images: Data Preparation and Detection Method. *Astrophys. J.* **823**, 53 (2016). DOI 10.3847/0004-637X/823/1/53.

65. Linker, J. A. *et al.* The Open Flux Problem. *Astrophys. J.* **848**, 70 (2017). DOI 10.3847/1538-4357/aa8a70.

66. Hannah, I. G. & Kontar, E. P. Differential emission measures from the regularized inversion of Hinode and SDO data. *Astron. Astrophys.* **539**, A146 (2012). DOI 10.1051/0004-6361/201117576.

67. Tomczyk, S. *et al.* Scientific objectives and capabilities of the Coronal Solar Magnetism Observatory. *Journal of Geophysical Research (Space Physics)* **121**, 7470–7487 (2016). DOI 10.1002/2016JA022871.

68. Landi, E., Young, P. R., Dere, K. P., Del Zanna, G. & Mason, H. E. CHIANTI—An Atomic Database for Emission Lines. XIII. Soft X-Ray Improvements and Other Changes. *Astrophys. J.* **763**, 86 (2013). DOI 10.1088/0004-637X/763/2/86.

69. Liu, Y. *et al.* Comparison of Line-of-Sight Magnetograms Taken by the Solar Dynamics Observatory/Helioseismic and Magnetic Imager and Solar and Heliospheric Observatory/Michelson Doppler Imager. *Sol. Phys.* **279**, 295–316 (2012). DOI 10.1007/s11207-012-9976-x.

70. Riley, P. *et al.* A Multi-Observatory Inter-Comparison of Line-of-Sight Synoptic Solar Magnetograms. *Sol. Phys.* **289**, 769–792 (2014). DOI 10.1007/s11207-013-0353-1.

71. Mikić, Z., Lionello, R., Mok, Y., Linker, J. A. & Winebarger, A. R. The Importance of Geometric Effects in Coronal Loop Models. *Astrophys. J.* **773**, 94 (2013). DOI 10.1088/0004-637X/773/2/94.

72. Linker, J. *et al.* MHD simulation of the Bastille day event. In *American Institute of Physics Conference Series*, vol. 1720 of *American Institute of Physics Conference Series*, 020002 (2016). DOI 10.1063/1.4943803.

73. Heinemann, M. & Olbert, S. Non-WKB Alfven waves in the solar wind. *J. Geophys. Res.* **85**, 1311–1327 (1980). DOI 10.1029/JA085iA03p01311.

74. Zank, G. P., Matthaeus, W. H. & Smith, C. W. Evolution of turbulent magnetic fluctuation power with heliospheric distance. *J. Geophys. Res.* **101**, 17093–17108 (1996). DOI 10.1029/96JA01275.

75. Zank, G. P. *et al.* The Transport of Low-frequency Turbulence in Astrophysical Flows. I. Governing Equations. *Astrophys. J.* **745**, 35 (2012). DOI 10.1088/0004-637X/745/1/35.

76. Velli, M. On the propagation of ideal, linear Alfven waves in radially stratified stellar atmospheres and winds. *Astron. Astrophys.* **270**, 304–314 (1993).

77. Dmitruk, P., Milano, L. J. & Matthaeus, W. H. Wave-driven Turbulent Coronal Heating in Open Field Line Regions: Nonlinear Phenomenological Model. *Astrophys. J.* **548**, 482–491 (2001). DOI 10.1086/318685.

78. Cranmer, S. R., van Ballegooijen, A. A. & Edgar, R. J. Self-consistent Coronal Heating and Solar Wind Acceleration from Anisotropic Magnetohydrodynamic Turbulence. *Astrophys. J. Suppl.* **171**, 520–551 (2007). DOI 10.1086/518001.

79. Verdini, A. & Velli, M. Alfvén Waves and Turbulence in the Solar Atmosphere and Solar Wind. *Astrophys. J.* **662**, 669–676 (2007). DOI 10.1086/510710.

80. Breech, B. *et al.* Turbulence transport throughout the heliosphere. *Journal of Geophysical Research (Space Physics)* **113**, 8105 (2008). DOI 10.1029/2007JA012711.

81. Chandran, B. D. G. & Hollweg, J. V. Alfvén Wave Reflection and Turbulent Heating in the Solar Wind from 1 Solar Radius to 1 AU: An Analytical Treatment. *Astrophys. J.* **707**, 1659–1667 (2009). DOI 10.1088/0004-637X/707/2/1659.

82. Usmanov, A. V., Matthaeus, W. H., Breech, B. A. & Goldstein, M. L. Solar Wind Modeling with Turbulence Transport and Heating. *Astrophys. J.* **727**, 84 (2011). DOI 10.1088/0004-637X/727/2/84.

83. Jin, M. *et al.* A Global Two-temperature Corona and Inner Heliosphere Model: A Comprehensive Validation Study. *Astrophys. J.* **745**, 6 (2012). DOI 10.1088/0004-637X/745/1/6.

84. Sokolov, I. V. *et al.* Magnetohydrodynamic Waves and Coronal Heating: Unifying Empirical and MHD Turbulence Models. *Astrophys. J.* **764**, 23 (2013). DOI 10.1088/0004-637X/764/1/23.

85. van der Holst, B. *et al.* Alfvén Wave Solar Model (AWSoM): Coronal Heating. *Astrophys. J.* **782**, 81 (2014). DOI 10.1088/0004-637X/782/2/81.

86. Oran, R. *et al.* A Steady-state Picture of Solar Wind Acceleration and Charge State Composition Derived from a Global Wave-driven MHD Model. *Astrophys. J.* **806**, 55 (2015). DOI 10.1088/0004-637X/806/1/55.

87. Cranmer, S. R. & van Ballegooijen, A. A. On the Generation, Propagation, and Reflection of Alfvén Waves from the Solar Photosphere to the Distant Heliosphere. *Astrophys. J. Suppl.* **156**, 265–293 (2005). DOI 10.1086/426507.

88. Verdini, A., Velli, M., Matthaeus, W. H., Oughton, S. & Dmitruk, P. A Turbulence-Driven Model for Heating and Acceleration of the Fast Wind in Coronal Holes. *Astrophys. J.* **708**, L116–L120 (2010). DOI 10.1088/2041-8205/708/2/L116.

89. de Karman, T. & Howarth, L. On the Statistical Theory of Isotropic Turbulence. *Royal Society of London Proceedings Series A* **164**, 192–215 (1938). DOI 10.1098/rspa.1938.0013.

90. Dobrowolny, M., Mangeney, A. & Veltri, P. Fully developed anisotropic hydromagnetic turbulence in interplanetary space. *Physical Review Letters* **45**, 144–147 (1980). DOI 10.1103/PhysRevLett.45.144.

91. Grappin, R., Leorat, J. & Pouquet, A. Dependence of MHD turbulence spectra on the velocity field-magnetic field correlation. *Astron. Astrophys.* **126**, 51–58 (1983).

92. Hossain, M., Gray, P. C., Pontius, D. H., Jr., Matthaeus, W. H. & Oughton, S. Phenomenology for the decay of energy-containing eddies in homogeneous MHD turbulence. *Physics of Fluids* **7**, 2886–2904 (1995). DOI 10.1063/1.868665.

93. Matthaeus, W. H. *et al.* Transport of cross helicity and radial evolution of Alfvénicity in the solar wind. *Geophys. Res. Lett.* **31**, 12803 (2004). DOI 10.1029/2004GL019645.

94. Vial, J. & Engvold, O. *Solar Prominences*. Astrophysics and Space Science Library (Springer International Publishing, 2015).

95. Yeates, A. R. *et al.* Global Non-Potential Magnetic Models of the Solar Corona During the March 2015 Eclipse. *Submitted to Space Sci. Rev.* (2017).

96. Mackay, D. H. & van Ballegooijen, A. A. Models of the Large-Scale Corona. I. Formation, Evolution, and Liftoff of Magnetic Flux Ropes. *Astrophys. J.* **641**, 577–589 (2006). DOI 10.1086/500425.

97. Yeates, A. R., Mackay, D. H. & van Ballegooijen, A. A. Modelling the Global Solar Corona II: Coronal Evolution and Filament Chirality Comparison. *Sol. Phys.* **247**, 103–121 (2008). DOI 10.1007/s11207-007-9097-0.

98. Mackay, D. H. & van Ballegooijen, A. A. A Non-Linear Force-Free Field Model for the Evolving Magnetic Structure of Solar Filaments. *Sol. Phys.* **260**, 321–346 (2009). DOI 10.1007/s11207-009-9468-9.

99. Karna, N., Hess Webber, S. A. & Pesnell, W. D. Using Polar Coronal Hole Area Measurements to Determine the Solar Polar Magnetic Field Reversal in Solar Cycle 24. *Sol. Phys.* **289**, 3381–3390 (2014). DOI 10.1007/s11207-014-0541-7.

100. Titov, V. S., Hornig, G. & Démoulin, P. Theory of magnetic connectivity in the solar corona. *Journal of Geophysical Research (Space Physics)* **107**, 1164 (2002). DOI 10.1029/2001JA000278.

101. Titov, V. S., Mikić, Z., Török, T., Linker, J. A. & Panasenco, O. 2010 August 1-2 Sympathetic Eruptions. I. Magnetic Topology of the Source-surface Background Field. *Astrophys. J.* **759**, 70 (2012). DOI 10.1088/0004-637X/759/1/70.

102. Titov, V. S., Mikić, Z., Török, T., Linker, J. A. & Panasenco, O. 2010 August 1-2 Sympathetic Eruptions. II. Magnetic Topology of the MHD Background Field. *Astrophys. J.* **845**, 141 (2017). DOI 10.3847/1538-4357/aa81ce.

103. Savcheva, A. S., van Ballegooijen, A. A. & DeLuca, E. E. Field Topology Analysis of a Long-lasting Coronal Sigmoid. *Astrophys. J.* **744**, 78 (2012). DOI 10.1088/0004-637X/744/1/78.

Acknowledgements

This research was supported by NASA (HSR and LWS programs), AFOSR, and the National Science Foundation (NSF). Z.M. acknowledges support from NASA grants NNX16AH03G and NNX15AB65G. Computations were provided by NASA's Advanced Supercomputing Division, NSF's Texas Advanced Computing Center, and San Diego Supercomputer Center. Data courtesy of NASA/SDO and the AIA and HMI science teams. We thank the International Space Science Institute in Bern, Switzerland, for hosting a team on "Global Non-Potential Magnetic Models of the Solar Corona," led by A. Yeates, where some of the ideas were developed. We thank the Solar Physics Group at Stanford University for their support in providing timely access to HMI data. Data courtesy of the Mauna Loa Solar Observatory, operated by the High Altitude Observatory, as part of the National Center for Atmospheric Research (NCAR). NCAR is supported by NSF. D.H.M. would like to thank both the UK STFC and the Leverhulme Trust for their financial support. L.A.U. was supported by the NSF Atmospheric and Geospace Sciences Postdoctoral Research Fellowship Program. The Williams College Eclipse Expedition was supported in large part by grants from the Solar Terrestrial Program of the Division of Atmospheric and Geospace Sciences of NSF and from the Committee for Research and Exploration of the National Geographic Society, with additional support from the NASA Massachusetts Space Grant Consortium, the Sigma Xi scientific research honor society, and the Clare Booth Luce Foundation.

Author contributions

Z.M. and C.D. wrote the text, developed and ran the MHD model, and analyzed the output. R.M.C. developed and ran the MHD model. D.H.M. ran the magnetofrictional model. L.U. analyzed data and provided model inputs. J.A.L., P.R., R.L., T.T., and V.S.T. contributed to the development of the MHD model. J.W., P.R., and Z.M. developed the web site. M.D. photographed the eclipse and produced an eclipse image. J.M.P. organized the 2017 eclipse expedition and its imaging, supervised the composition of an eclipse image, and contributed to the text. W.C. composed an eclipse image. All authors reviewed the manuscript.

Additional information

Reprints and permissions information is available at www.nature.com/reprints.
The authors declare no competing financial interests.
Correspondence and requests for materials should be addressed to mikicz@predsci.com.

Predicting the Corona for the 21 August 2017 Total Solar Eclipse

Zoran Mikić[1], Cooper Downs[1], Jon A. Linker[1], Ronald M. Caplan[1],
Duncan H. Mackay[2], Lisa A. Upton[3], Pete Riley[1], Roberto Lionello[1],
Tibor Török[1], Viacheslav S. Titov[1], Janvier Wijaya[1],
Miloslav Druckmüller[4], Jay M. Pasachoff[5,6], and Wendy Carlos[7]

Supplementary Information:
Notes and Figures

[1]Predictive Science, Inc., San Diego, CA 92121, USA

[2]School of Mathematics and Statistics, University of St Andrews, St Andrews, Fife, KY16 9SS, UK

[3]High Altitude Observatory, National Center for Atmospheric Research, Boulder, CO 80301, USA

[4]Institute of Mathematics, Faculty of Mechanical Engineering, Brno University of Technology, Czech Republic

[5]Williams College–Hopkins Observatory, Williamstown, MA 01267, USA

[6]Carnegie Observatories, Pasadena, CA 91101, USA

[7]New York City, NY 10003, USA

Supplementary Notes

Supplementary Note 1: Treatment of Polar Fields

The high-latitude radial magnetic field B_r estimated from HMI line-of-sight synoptic maps has inaccuracies due to projection effects. We therefore used a fitting procedure to specify B_r in the polar caps. The time interval during which the synoptic map was assembled from central meridian observations, 16 July–11 August 2017, includes a large part of Carrington rotation (CR) 2193 and a small part of CR 2192, as shown in Supplementary Figure 2. During that time, the solar B_0 angle varied between 4.4° and 6.4°, implying that the north pole of the Sun was visible from Earth, and that the south pole was hidden. We used a geometrical fitting of the high-latitude field (in the latitude region 67°–79°N for the north pole, and 53°–67°S for the south pole) to estimate the polar field (Linker et al. 2013). We verified that this field was consistent with estimates made for previous rotations when the respective poles were maximally visible from Earth, since we keep a running record of the polar fields over time. Alternate schemes for estimating polar fields have also been developed (Sun et al. 2011; Sun 2018). The existing values of B_r from the HMI synoptic map were replaced in the region with latitudes between 80°–90°N and 73°–90°S as follows. To make the polar field less smooth the flux was concentrated into small localized flux elements (Tsuneta et al. 2008), using ~ 400 small flux patches in the north polar cap and ~ 150 in the south polar cap, picked randomly in strength from a Gaussian distribution whose mean matched the fitted values. The total flux in these caps was equivalent to a magnetic field of 2.9 G at the north pole, and -4.3 G at the south pole (before scaling of the overall field by the factor of 1.4, as explained in the Methods section). This field was spatially smoothed using a low-pass filter to blend it with the measured high-latitude field, to give the final result, as shown in Supplementary Figure 2. Flux transport models (e.g., Yeates 2014; Nandy et al. 2018) offer promising alternatives for estimating polar fields.

Supplementary Note 2: Volume Rendering of Q

The volume rendering of the squashing factor Q of magnetic flux tubes was performed as follows. For the large field-of-view images (Figures 1d, 3b, and 3c), the integral takes the form

$$\int_{LOS} e^{-s^2/(2r^2\sigma^2)}\, r^{-n} \log_{10} Q\, ds,$$

where the integration is along the LOS coordinate, s, which is perpendicular to the plane-of-sky, with $s = 0$ corresponding to the limb. The Gaussian term weights the integration to a certain angular extent away from the plane-of-sky, with σ chosen to give a FWHM of 40°. The r^{-n} term influences the weighting of structures as a function of height in the solar atmosphere, with $n = 1$ corresponding to equal weighting. To separate low-, mid-, and large-scale coronal heights, we use

different powers of $n = 3$, $n = 2$, and $n = 1.5$ for the respective R, G, and B color channels. The signal for each channel is converted to image intensity using linear scaling.

The smaller field-of-view images (Figures 3d, and 4d, and Supplementary Figure 6) are designed to emphasize low coronal structures over the solar disk and off the solar limb. Here the integral uses simple exponential weighting,

$$\int_{LOS} e^{-r/\lambda} \log_{10} Q \, ds,$$

where λ is a scale height. To separate features at different heights we choose $\lambda = 21\,\mathrm{Mm}$, $\lambda = 84\,\mathrm{Mm}$, and $\lambda = 140\,\mathrm{Mm}$, respectively, for the R, G, and B color channels. The signal for each channel is converted to image intensity using logarithmic scaling.

Supplementary References

Linker, J. A., Mikić, Z., Riley, P., Downs, C., Lionello, R., Henney, C., and Arge, C. N. (2013). Coronal and heliospheric modeling using flux-evolved maps. In Zank, G. P. et al., editors, *SOLAR WIND 13: Proceedings of the Thirteenth International Solar Wind Conference, June 17-22, 2012*, volume 1539 of *American Institute of Physics Conference Series*, pages 26–29.

Nandy, D., Bhowmik, P., Yeates, A. R., Panda, S., Tarafder, R., and Dash, S. (2018). The Large-scale Coronal Structure of the 2017 August 21 Great American Eclipse: An Assessment of Solar Surface Flux Transport Model Enabled Predictions and Observations. *Astrophys. J.*, **853**, 72.

Sun, X. (2018). Polar Field Correction for HMI Line-of-Sight Synoptic Data. Preprint at http://arxiv.org/abs/1801.04265.

Sun, X., Liu, Y., Hoeksema, J. T., Hayashi, K., and Zhao, X. (2011). A New Method for Polar Field Interpolation. *Sol. Phys.*, **270**, 9–22.

Tsuneta, S., Ichimoto, K., Katsukawa, Y., Lites, B. W., Matsuzaki, K., Nagata, S., Orozco Suárez, D., Shimizu, T., Shimojo, M., Shine, R. A., Suematsu, Y., Suzuki, T. K., Tarbell, T. D., and Title, A. M. (2008). The Magnetic Landscape of the Sun's Polar Region. *Astrophys. J.*, **688**, 1374–1381.

Yeates, A. R. (2014). Coronal Magnetic Field Evolution from 1996 to 2012: Continuous Non-potential Simulations. *Sol. Phys.*, **289**, 631–648.

Supplementary Figures

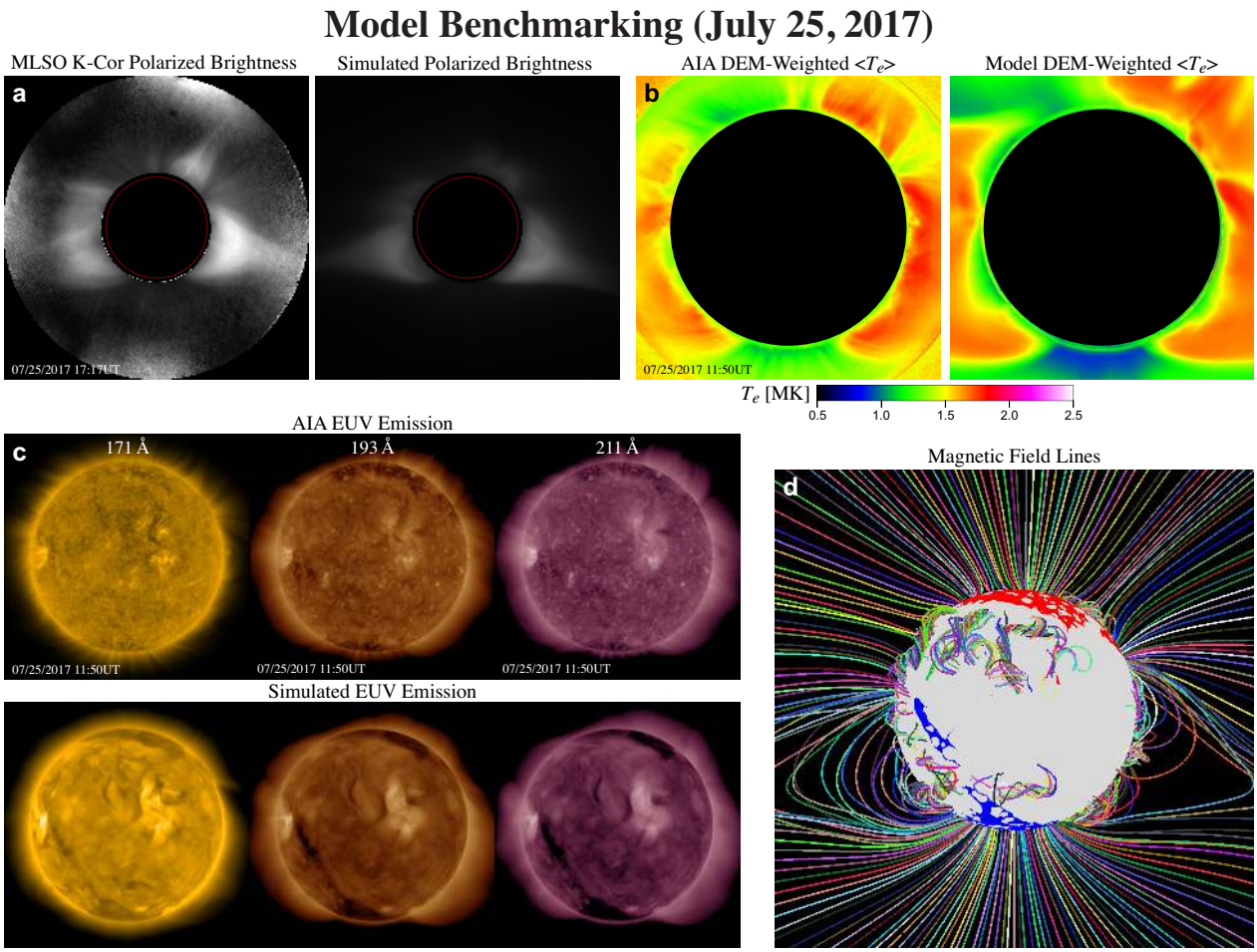

Supplementary Figure 1. Comparison of predicted and simulated quantities during model benchmarking. An example of a comparison with observations on 25 July 2017, one solar rotation prior to the eclipse. **a**, A 30-minute average of MLSO K-Cor pB compared with simulated pB; the same scaling and (Newkirk) radial filter is used for both images. **b**, Average DEM-weighted off-limb electron temperature for the observed and simulated data, derived by integrating over the 6-channel AIA DEM fit. **c**, Comparison of AIA 171 Å, 193 Å, and 211 Å EUV emission with simulated images. **d**, Selected magnetic field lines from the model, highlighting the streamer structure in the plane of the sky, and showing open-field (blue and red) and closed-field (gray) areas in the photosphere.

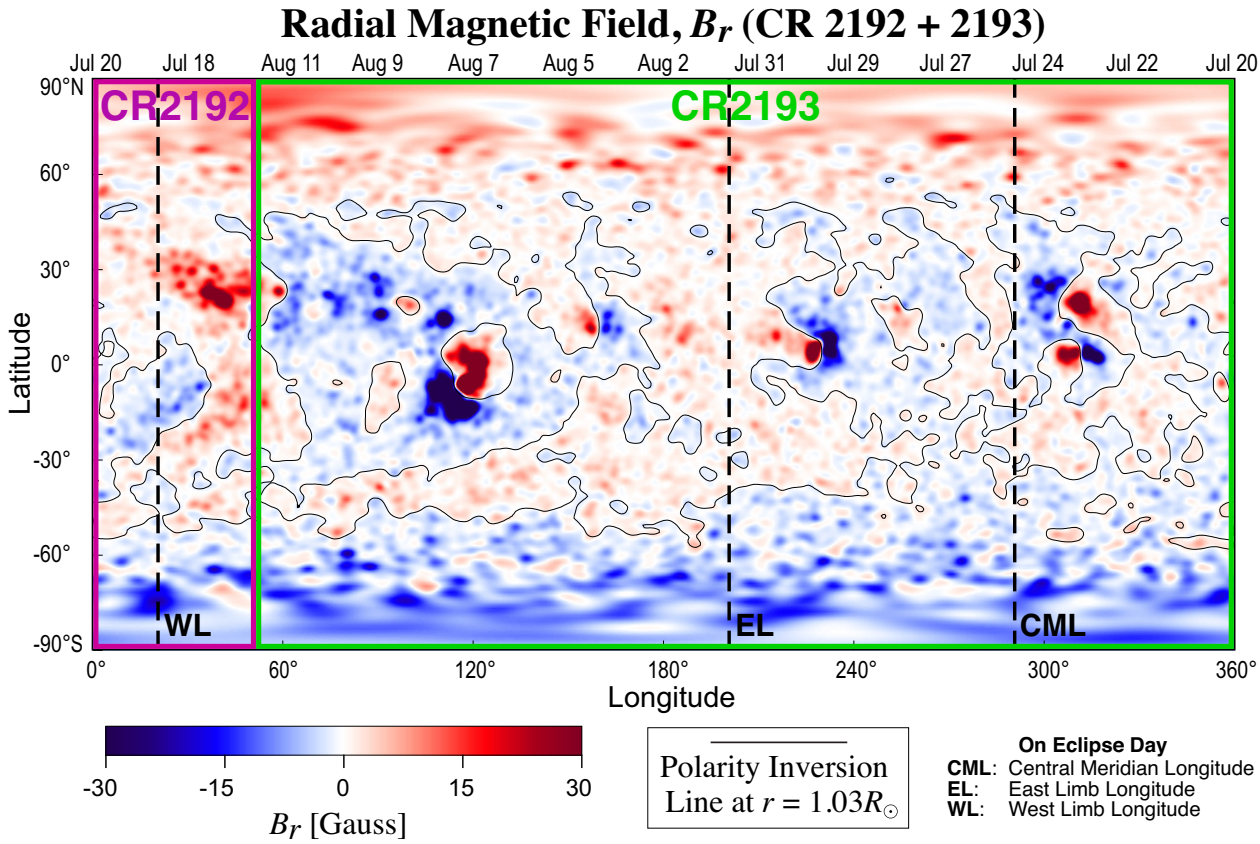

Supplementary Figure 2. Photospheric magnetic field. Synoptic chart of the radial component of the photospheric magnetic field, B_r, for CR 2192 + 2193, measured by HMI and scaled by the factor 1.4, that was used for the final prediction. The dates at the top of the image show the time when the data was measured at central meridian. The dashed vertical black lines show the longitudes of the central meridian (CML), the east limb (EL), and the west limb (WL) at eclipse time.

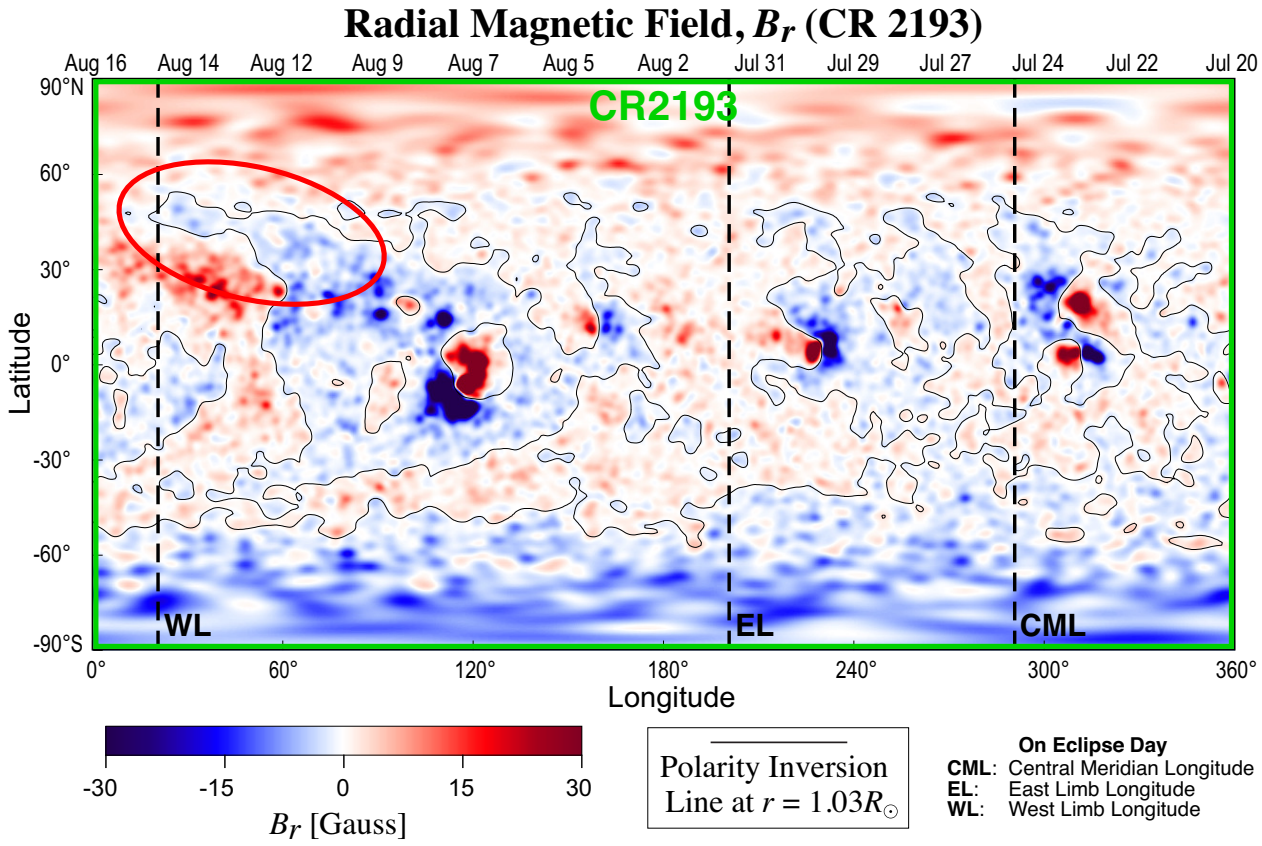

Supplementary Figure 3. Updated photospheric magnetic field. Synoptic chart of B_r for CR 2193. The magnetic field data near the west limb (longitudes 0°–51°) is updated to 12–16 August 2017, compared to the data in the chart for CR 2192 + 2193, which was measured during 16–20 July 2017 at those locations, shown in Supplementary Figure 2. Note that the negative polarity region (blue) near latitude 50°N (inside the red oval) now extends to the west limb (WL), supporting the formation of a pseudostreamer there. A comparison between the polarity inversion line (PIL) for this data and the data for CR 2192 + 2193 is shown in Figure 5.

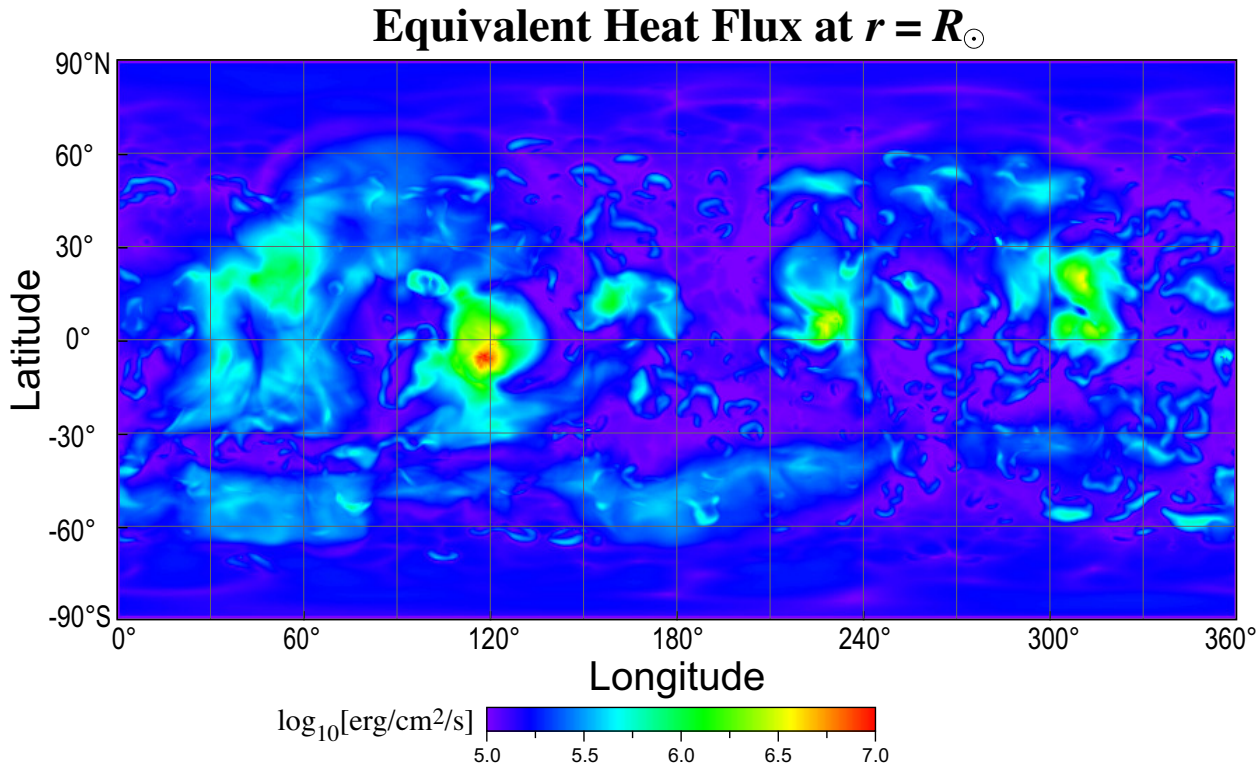

Supplementary Figure 4. Equivalent heat flux. A synoptic map of the equivalent heat flux at $r = R_\odot$, using a logarithmic scale, for the final eclipse prediction.

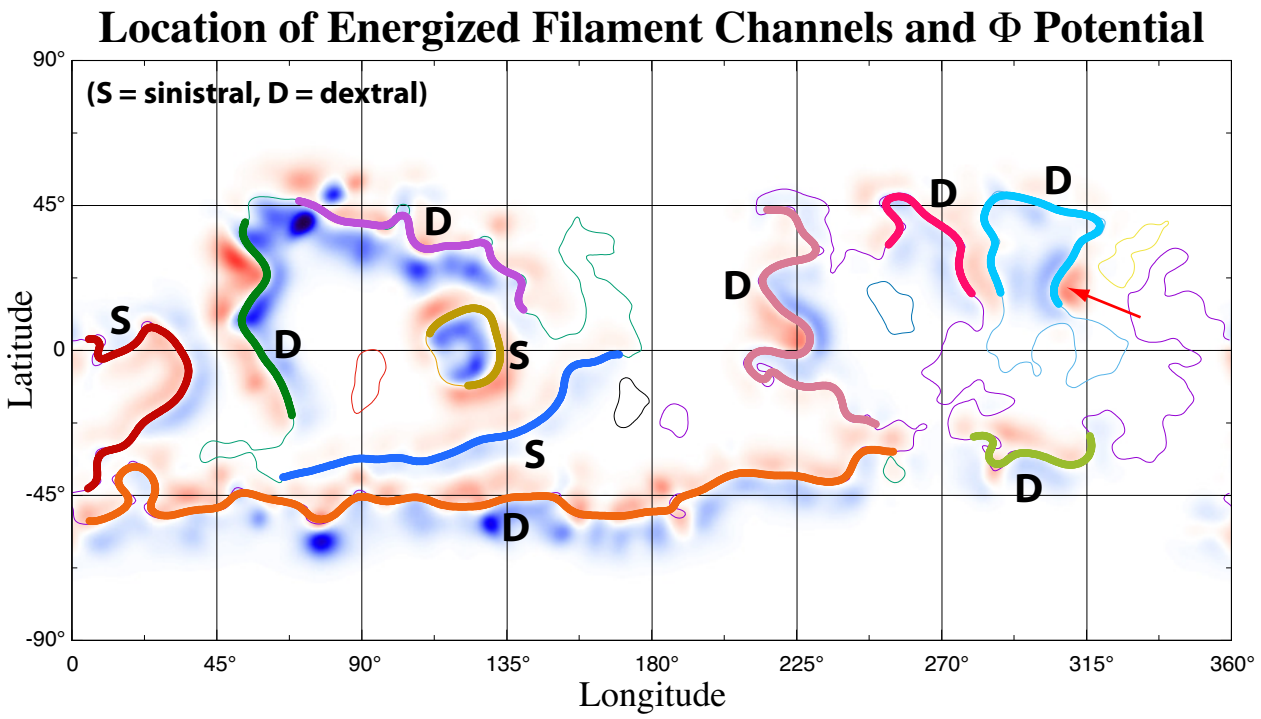

Supplementary Figure 5. Locations of energized filament channels. The synoptic map shows the Φ potential that was used to energize the magnetic field, with blue (red) indicating negative (positive) values. The thin line shows the PIL at $r = 1.05R_{\odot}$, and the colored segments show the locations of the filament channels that were energized, as determined from AIA observations. The chirality of the magnetic field (sinistral or dextral) was determined from a separate run of the magnetofrictional model. The red arrow near latitude 22°N, longitude 305° indicates the section of the PIL that passes through the active region that appears in the northwest of the solar disk on 25 July 2017, shown in Figure 2. An animation that fades the locations of the energized filament channels on a background image of a synoptic map of observed AIA 193 Å emission is shown in Supplementary Video 9.

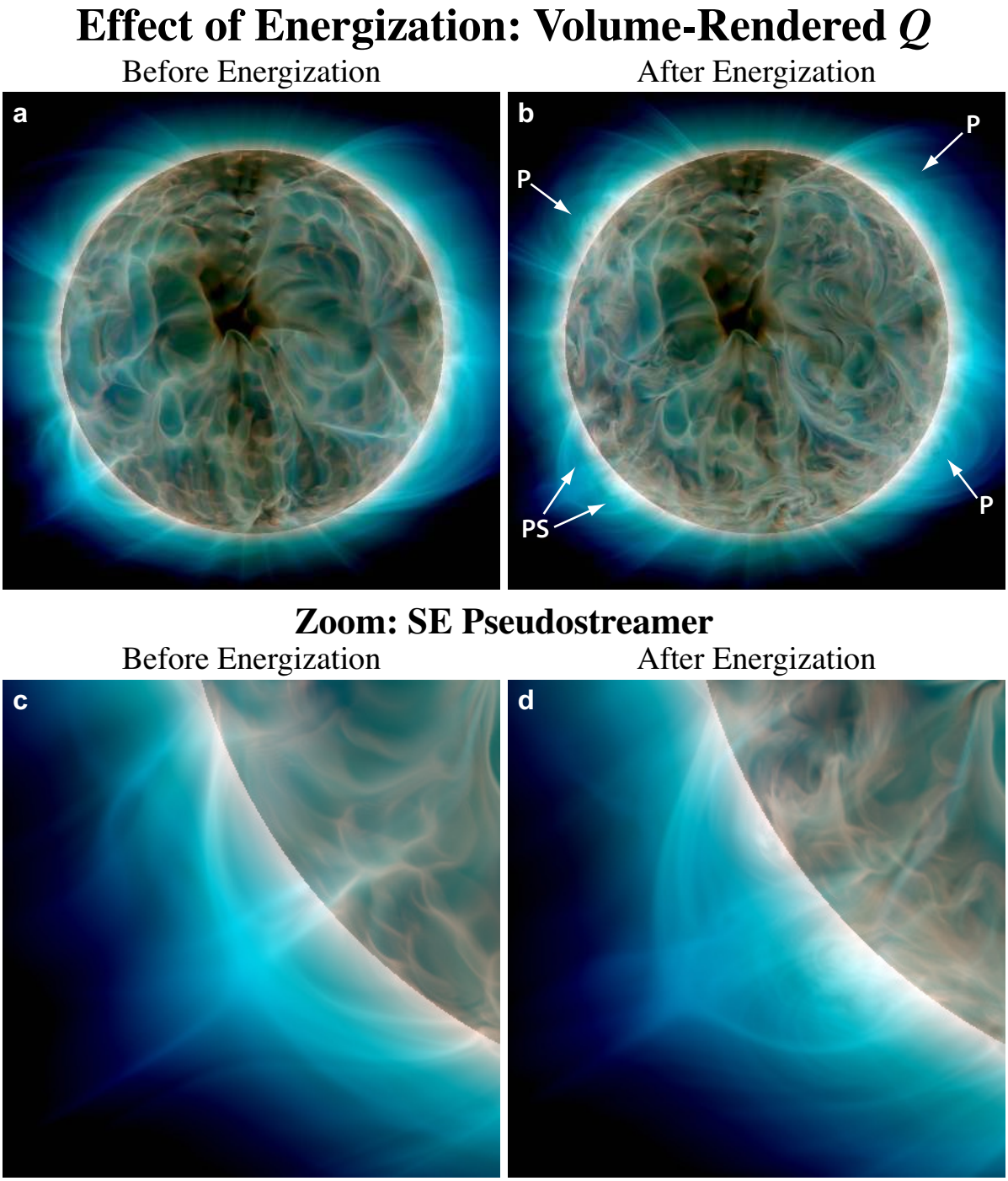

Supplementary Figure 6. Energization of the magnetic field. Volume-rendered squashing factor Q at 18:02 UT on 1 August 2017, before energization of the magnetic field, **a** and **c**, and after energization, **b** and **d**. The twisted flux ropes in the energized model visibly inflate the streamers on the limb at locations of prominences (P) and in the pseudostreamer (PS). This is the same view as that shown in Figure 4. Supplementary Video 8 shows an animation that fades between images **a** and **b**.

Supplementary Videos

- **Supplementary Video 1.** An animation of the simulated polarized brightness versus central meridian longitude, showing the 3D structure of the streamers around the Sun. The time of eclipse in Oregon corresponds to a central meridian longitude (CML) of 290.7°. (For the best effect, when viewing this movie, set your video player to loop continuously.)

- **Supplementary Video 2.** An animation that fades between an observed eclipse image (Fig. 1a) and the magnetic field lines (Fig. 1e). (For the best effect, when viewing this movie, set your video player to loop continuously.)

- **Supplementary Video 3.** An animation of the large field-of-view squashing factor Q versus central meridian longitude, showing the 3D structure of the large-scale magnetic field around the Sun. (For the best effect, when viewing this movie, set your video player to loop continuously.)

- **Supplementary Video 4.** An animation that fades between an observed eclipse image (Fig. 1a) and the squashing factor Q (Fig. 1d). (For the best effect, when viewing this movie, set your video player to loop continuously.)

- **Supplementary Video 5.** An animation that fades between an observed eclipse image (Fig. 1a) and the simulated polarized brightness pB (Fig. 1c). (For the best effect, when viewing this movie, set your video player to loop continuously.)

- **Supplementary Video 6.** An animation of the small field-of-view squashing factor Q, showing the 3D structure of the magnetic field in the inner corona. (For the best effect, when viewing this movie, set your video player to loop continuously.)

- **Supplementary Video 7.** An animation of the magnetic field lines as the Sun rotates, showing the open- and closed-field regions, as well as the twisted flux ropes in the filament channels. (For the best effect, when viewing this movie, set your video player to loop continuously.)

- **Supplementary Video 8.** An animation that fades between the squashing factor Q in the inner corona for the unenergized (Supplementary Fig. 6a) and energized (Supplementary Fig. 6b) corona on 1 August 2017. Note that the twisted flux ropes in the filament channels (in the energized model) visibly inflate the streamers and the pseudostreamer. (For the best effect, when viewing this movie, set your video player to loop continuously.)

- **Supplementary Video 9.** An animation that fades the locations of the energized filament channels (colored lines from Supplementary Fig. 5) on a background image of a synoptic map of observed AIA 193 Å emission for CR 2192 + 2193 (16 July–12 August 2017). (For the best effect, when viewing this movie, set your video player to loop continuously.)